

Geometric Framework for Robust Order Detection in Delay-Coordinates Dynamic Mode Decomposition

Yoav Harris,^{1, a)} Hadas Benisty,² and Ronen Talmon¹

¹⁾Viterbi Faculty of Electrical and Computer Engineering, Technion – Israel Institute of Technology, Haifa 3200003, Israel

²⁾Rappaport Faculty of Medicine, Technion – Israel Institute of Technology, Haifa 3200003, Israel

Delay-coordinates dynamic mode decomposition (DC–DMD) is widely used to extract coherent spatiotemporal modes from high-dimensional time series. A central challenge is distinguishing dynamically meaningful modes from spurious modes induced by noise and order overestimation. We show that model order detection and mode selection in DC–DMD are fundamentally problems of subspace geometry. Specifically, true modes are characterized by concentration within a low-dimensional signal subspace, whereas spurious modes necessarily retain non-negligible components outside any moderate overestimate of that subspace. This geometric distinction yields a perturbation-robust definition of true and spurious modes and yields fully data-driven selection criteria. This geometric framework leads to two complementary data-driven selection criteria. The first is derived directly from the geometric distinction and uses a data-driven proxy of the signal-subspace to compute a residual score. The second arises from a new operator-theoretic analysis of delay embedding. Using a block-companion formulation, we show that all modes exhibit a Kronecker–Vandermonde (KV) structure induced by the delay-coordinates, and true modes are distinguished by the degree to which they conform to it. Importantly, we also show that this deviation is governed precisely by the geometric residual. In addition, our analysis provides a principled explanation for the empirical behavior of magnitude- and norm-based heuristics, clarifying when and why they fail under delay-coordinates. Extensive numerical experiments confirm the theoretical predictions and demonstrate that the proposed geometric and structure-based methods achieve robust and accurate order detection and mode selection, consistently better than existing baselines across noise levels, spectral separations, damping regimes, and embedding lengths.

Delay-coordinates dynamic mode decomposition (DC–DMD) is a widely-used tool for extracting coherent patterns from noisy, high-dimensional time series, but in practice it often returns more candidate components than truly reflect the underlying dynamics. The central challenge is to determine which recovered modes are physically meaningful and which are artifacts of noise and order overestimation. In this work, we show that this problem can be understood through subspace geometry, leading to a data-driven residual criterion that distinguishes true from spurious modes. We further show that delay coordinates impose a characteristic internal organization on the recovered modes, yielding a complementary structure-based selection criterion. This geometric framework also clarifies why commonly used magnitude- and norm-based heuristics can become unreliable. Together, these results provide a more interpretable and robust framework for order detection and mode selection in DC–DMD.

I. INTRODUCTION

High-dimensional time series arise in a wide range of physical and biological systems, including fluid flows^{1,2}, neural recordings^{3,4}, climate dynamics^{5,6}, and mechanical systems^{7,8}. Such time series are inevitably contaminated by noise and unmodeled effects. Although the data may involve many ob-

servables, the underlying dynamics are often governed by a relatively small number of coherent components. A central challenge in data-driven dynamical analysis is therefore to extract these latent components and characterize their temporal behavior directly from observed trajectories⁹.

Dynamic Mode Decomposition (DMD) is a widely used framework for this purpose. Originally introduced in the context of fluid dynamics, DMD approximates the observed temporal evolution by a best-fit linear operator learned from sampled data and interprets its eigenpairs as spatiotemporal building blocks of the underlying dynamics^{1,10,11}. The associated eigenvalues encode oscillatory and growth or decay behavior, while the corresponding modes, which are constructed from the eigenvectors, encode spatial structure. Variants of DMD and related operator-theoretic methods have since been applied across many scientific and engineering domains^{12–14}.

From an operator-theoretic perspective, DMD can be interpreted as a finite-dimensional, data-driven approximation of the Koopman operator, which provides a linear representation of nonlinear dynamics through its action on observables^{15–18}. This connection becomes particularly natural under lifting strategies that enrich the observable space and expose additional spectral content.

A common enhancement of DMD is the use of *delay coordinates*, where snapshot matrices are formed by stacking time-delayed samples into each column. This approach provides a systematic means of expanding the space of observables, improving spectral resolution, and strengthening the link between data-driven linear models and Koopman operator theory^{19–21}. Delay coordinates originate in nonlinear dynamics and attractor reconstruction²², and are closely related

^{a)}Electronic mail: yoav.h@campus.technion.ac.il

to classical subspace identification, Hankel-based techniques, and matrix pencil methods^{23,24}. In the context of DMD, delay-coordinates formulations, often referred to as Hankel-DMD or Delay-Coordinates Dynamic Mode Decomposition (DC-DMD), have been shown to enhance mode separation and recover more accurate spectral information from short or noisy time series^{10,25–28}. One concrete illustration is the standing-wave case, where a single real oscillation is generated by a pair of complex-conjugate components. In this setting, standard DMD (without delay coordinates) often splits the oscillation into two separate modes whose individual spatial patterns are not physically meaningful, whereas DC-DMD recovers the correct oscillatory structure²⁹.

In the presence of noise, the snapshot matrices formed in DC-DMD are effectively full rank, and hence, practical implementations typically work with truncation rank that only approximates the unknown true model order. When the model order is overestimated, the computed decomposition necessarily includes additional components that have no counterpart in the underlying dynamics.

The problem of identifying which DMD components reflect true dynamics, and which are spurious artifacts of noise and order overestimation, has therefore received considerable attention. Existing approaches include spectral heuristics^{10,11}, likelihood- and information-theoretic criteria^{30–32}, robustness-based methods^{33,34}, and structure-aware post hoc tests that exploit delay-induced spatiotemporal structure²⁹. Importantly, in delay-coordinate settings, detecting the model order becomes more challenging. As we show in the sequel, delay coordinates induce spatiotemporal organization in the lifted space, where the spurious additional components appear coherent across delays, and therefore, become more difficult to separate from true modes than in standard (non-delayed) DMD; as a result, common heuristics such as singular-value gap rules, eigenvalue screening, or mode-norm rankings become unreliable.

Despite the extensive body of work, order detection in DC-DMD lacks a principled, perturbation-robust definition of what distinguishes a true dynamical component from a spurious one. Existing approaches largely treat spurious modes as residual artifacts of noise or overfitting, without explicitly characterizing their structural relationship to the signal-dominated subspaces induced by the data. As a result, selection rules are typically formulated in terms of spectral magnitude, likelihood penalties, or empirical stability, rather than in terms of intrinsic geometric properties of the recovered modes.

In this paper, we argue that order detection in DC-DMD is fundamentally a problem of subspace geometry. True modes are those that concentrate their energy within a low-dimensional signal subspace, while spurious modes necessarily retain non-negligible components outside any moderate overestimate of this subspace. This geometric distinction yields a perturbation-robust definition of true and spurious modes and leads directly to practical selection algorithms.

Building on this geometric framework, we develop two complementary mode-selection algorithms. The first translates the signal-subspace concentration principle into a fully data-driven residual score by constructing a proxy for the signal subspace and quantifying each mode’s deviation from it.

The second algorithm builds on a structural analysis of delay-coordinate modes. Prior work has identified a Kronecker–Vandermonde (KV) structure in true DC-DMD modes under explicit exponential signal models²⁹. Here, we show that this structure does not arise from the signal model itself, but is instead induced by the delay-coordinates and the block-companion structure of the least-squares propagator. In particular, we prove that all DMD modes, true and spurious, inherit an intrinsic KV organization, and that the distinguishing feature of true modes is not the presence of KV structure, but the degree to which they conform to it. This observation shifts the interpretation of KV structure from a binary signature of true components to a continuous structural property governed by subspace geometry. The deviation from ideal KV structure is shown to be directly controlled by the geometric residual introduced earlier, yielding a principled structural score for mode selection.

Finally, our analysis provides a principled explanation for the empirical behavior of commonly used mode-energy and mode-norm heuristics. By decomposing the exact-mode norm into eigenvalue-dependent and residual-dependent contributions, we show that delay coordinates fundamentally alter the spectral statistics of spurious modes. In particular, as the embedding length grows, spurious eigenvalues concentrate near the unit circle, rendering magnitude- and norm-based rankings unreliable or even misleading in weakly damped regimes. This clarifies when such heuristics can be expected to fail, and why residual- and structure-based criteria provide more robust alternatives in delay-coordinate settings.

We validate our theoretical analysis and algorithms through extensive numerical experiments covering a wide range of operating regimes, including varying noise levels, spectral separation, damping, amplitude heterogeneity, and embedding length. Across all tested scenarios, the proposed geometric and structure-based criteria yield significantly more reliable order detection than commonly used baselines, including spectral gap rules, information-theoretic criteria, robustness-based methods, and mode-norm heuristics. In particular, the experiments confirm the theoretical predictions that delay coordinates fundamentally alter the behavior of spurious components; as the embedding length increases, spurious eigenvalues concentrate near the unit circle, and spurious modes increasingly exhibit structured KV-like organization, causing magnitude- and energy-based rankings to degrade. In contrast, the proposed residual- and structure-based scores remain stable and discriminative, accurately separating true and spurious modes even in regimes where traditional heuristics fail.

The remainder of this paper is organized as follows. Section II formulates the setting, including the signal and delay-coordinate model, the DMD construction, the signal subspace, and the geometric order-detection viewpoint. Section III reviews related order-detection methods. Sections IV and V develop the geometric and structure-based criteria, respectively, and Section VI interprets common heuristics through this framework. Section VII presents numerical results, and Section VIII concludes with a summary and implications.

II. PROBLEM FORMULATION

In this section, we formalize the DC–DMD setting in a form suitable for geometric analysis. We introduce the signal model, the associated signal subspace, and the rank-constrained DMD construction, emphasizing the subspace relationships that underlie the distinction between true and spurious dynamical modes and our subsequent theoretical analysis and proposed algorithms.

A. System and signal model

We observe a signal in discrete time given by:

$$\mathbf{x}_k = \mathbf{s}_k + \mathbf{n}_k \in \mathbb{C}^D, \quad (1)$$

where \mathbf{n}_k represents noise, \mathbf{s}_k follows a deterministic time-evolution rule given by:

$$\mathbf{s}_{k+1} = f(\mathbf{s}_k), \quad \mathbf{s}_k \in \mathbb{C}^D, \quad (2)$$

and k is the discrete time index. Given the signal model (1) and the latent dynamical evolution (2), our objective is to recover the latent dynamics from a finite snapshot of N consecutive noisy observation samples $\{\mathbf{x}_k\}_{k=0}^{N-1}$.

We pursue two complementary outcomes: (i) recover the map f in (2) when it is identifiable from the data; or (ii) when full identification is not possible, obtain a faithful characterization of the dynamics, such as its dominant frequencies, growth or decay rates, and spatial structures. Such representations support tasks including denoising, by separating \mathbf{s}_k from \mathbf{n}_k , and prediction, by forecasting \mathbf{s}_{k+h} beyond the observation snapshot.

B. Delay-coordinates DMD

DMD and related methods commonly use delay-coordinates where each delay vector stacks L consecutive samples:

$$\tilde{\mathbf{x}}_k := \begin{bmatrix} \mathbf{x}_k \\ \mathbf{x}_{k+1} \\ \vdots \\ \mathbf{x}_{k+L-1} \end{bmatrix} \in \mathbb{C}^{DL}, \quad k = 0, \dots, N-L. \quad (3)$$

We define $\tilde{\mathbf{s}}_k$ and $\tilde{\mathbf{n}}_k$ similarly. Collecting all the delay vectors yields

$$\mathbf{X}^{(L)} := [\tilde{\mathbf{x}}_0 \cdots \tilde{\mathbf{x}}_{N-L}] = \mathbf{S}^{(L)} + \mathbf{E}^{(L)} \in \mathbb{C}^{DL \times (N-L)}. \quad (4)$$

In the remainder of this paper, unless explicitly stated otherwise, we fix $L \geq 1$ and, for brevity, we omit the superscript and write $\mathbf{X}, \mathbf{S}, \mathbf{E}$ for $\mathbf{X}^{(L)}, \mathbf{S}^{(L)}, \mathbf{E}^{(L)}$.

Classical delay–embedding theory shows that, under generic conditions, a delay map embeds the underlying attractor²², providing a standard basis for using delay-coordinates to enrich observed dynamics. In practice, delay-coordinates are widely

used to improve modal separation and spectral resolution in data-driven analysis of dynamical systems^{10,23,25,26}.

DMD approximates the temporal evolution map f from (2) by a linear propagator:

$$\mathbf{s}_{k+1} = \mathbf{A} \mathbf{s}_k. \quad (5)$$

Any trajectory of (5) admits a finite modal representation of the form:

$$\mathbf{s}_k = \sum_{j=1}^m b_j \phi_j \lambda_j^k = \mathbf{\Phi} \mathbf{\Lambda}^k \mathbf{b}, \quad (6)$$

where (λ_j, ϕ_j) are eigenpairs of \mathbf{A} , b_j are the amplitudes determined by the initial condition \mathbf{s}_0 , and m is the model order. Throughout, we parameterize the complex eigenvalues as

$$\lambda_j = \rho_j e^{i\theta_j}, \quad \rho_j \in [0, 1], \quad (7)$$

where ρ_j are magnitudes, θ_j are phases, and $\rho_j \leq 1$ ensures bounded temporal behavior. The triplets $(\rho_j, \theta_j, \phi_j)$ together with b_j are the signal parameters; throughout, we refer to them as the true underlying signal components. This modal form holds exactly when \mathbf{A} is diagonalizable. In the non-diagonalizable case, polynomial-exponential dynamics are typically represented in finite-data DMD by clusters of nearby simple eigenvalues; see^{10,11,25}.

Since the delay-coordinates embedding in (3) is linear, the linear evolution of \mathbf{s}_k carries over to the embedded vectors, motivating the approximation

$$\tilde{\mathbf{x}}_{k+1} \approx \mathbf{A} \tilde{\mathbf{x}}_k. \quad (8)$$

To estimate a one-step propagator, we pair each delay vector with its immediate successor and form two snapshot matrices

$$\begin{aligned} \mathbf{X}_0 &= [\tilde{\mathbf{x}}_0 \ \tilde{\mathbf{x}}_1 \ \cdots \ \tilde{\mathbf{x}}_{N-L-1}], \\ \mathbf{X}_1 &= [\tilde{\mathbf{x}}_1 \ \tilde{\mathbf{x}}_2 \ \cdots \ \tilde{\mathbf{x}}_{N-L}], \end{aligned} \quad (9)$$

both of size $DL \times (N-L)$. An analogous construction defines $\mathbf{S}_0, \mathbf{S}_1, \mathbf{E}_0, \mathbf{E}_1$, following (4).

The paired snapshot matrices satisfy $\text{rank}(\mathbf{S}_0) = \text{rank}(\mathbf{S}_1) = m$, since all their columns lie in $\text{span}\{\phi_1, \dots, \phi_m\}$. We therefore use “order” and “signal rank” interchangeably. As is typical in a wide range of systems, the number of underlying dynamical components is substantially smaller than the number of observables, so we adopt the standard assumption that

$$m \ll \min(N-L, DL).$$

The maximal algebraic rank of the signal matrices is $\min(N-L, DL)$. We focus on the common regime $N-L < DL$ (the complementary case $DL < N-L$ is less common and discussed in Appendix A).

Although the linear evolution is postulated for the latent signal, $\mathbf{S}_1 = \mathbf{A} \mathbf{S}_0$, in practice we estimate \mathbf{A} from the noisy observations by solving $\mathbf{X}_1 \approx \mathbf{A} \mathbf{X}_0$.

Noise affects the estimation process in two coupled ways: additive noise both perturbs the signal subspace and introduces directions that are not aligned with any low-dimensional signal geometry, thereby complicating the separation between signal-consistent and noise-consistent components. In particular, by our signal model (1), we have $\mathbf{X} = \mathbf{S} + \mathbf{E}$, where the additive noise \mathbf{E} obscures the low-rank structure of the signal \mathbf{S} , rendering \mathbf{X}_0 and \mathbf{X}_1 effectively full rank. Consequently, the true order m cannot be inferred from the ranks of the snapshot matrices alone. Because the true order m is unknown, we compute DMD at a working rank $M \geq m$, typically chosen strictly larger than m . This overestimation introduces additional components that have no signal counterpart and must be separated from the true modes.

Whether M coincides with m , and how deviations between them manifest, lies at the core of this work and is formalized as an *order detection* problem in Section II C.

Given the paired snapshot matrices $(\mathbf{X}_0, \mathbf{X}_1)$, a natural unconstrained least-squares solution, via the Moore–Penrose pseudoinverse^{35,36}, is

$$\widehat{\mathbf{A}}_{\text{MP}} = \mathbf{X}_1 \mathbf{X}_0^\dagger \quad (10)$$

However, in the presence of noise, this produces a (numerically) full-rank operator that absorbs high-variance directions and thereby *models noise as dynamics*. This undermines the identifiability of the true components. The low-rank assumption motivates solving a rank-constrained least squares:

$$\widehat{\mathbf{A}} = \arg \min_{\substack{\mathbf{A} \in \mathbb{C}^{DL \times DL} \\ \text{rank}(\mathbf{A})=M}} \|\mathbf{X}_1 - \mathbf{A}\mathbf{X}_0\|_F^2 \quad (11)$$

Broadly, DMD extracts the eigenpairs of the estimated propagator $\widehat{\mathbf{A}}$ from the rank-constrained least squares (11). Constraining the rank in (11) enforces the low-rank signal model, restricting the fit to an M -dimensional subspace. Geometrically, this restriction confines the fitted dynamics to an M -dimensional truncation subspace, which ideally contains the signal subspace \mathcal{S} , but may also include additional noise-aligned directions. This yields an explicit spatiotemporal representation, where the eigenvalues capture temporal evolution while the eigenvectors capture spatial structure. In this form, the signal can be modeled and reconstructed directly, rather than merely advanced one step by $\widehat{\mathbf{A}}$.

The practical solution to the rank-constrained least-squares problem (11) uses the truncated Singular Value Decomposition (SVD) of \mathbf{X}_0 (with truncation rank M):

$$\begin{aligned} \mathbf{X}_0 &\approx \mathbf{U}_M \boldsymbol{\Sigma}_M \mathbf{V}_M^H, \\ \mathbf{U}_M &\in \mathbb{C}^{DL \times M}, \quad \boldsymbol{\Sigma}_M \in \mathbb{R}^{M \times M}, \quad \mathbf{V}_M \in \mathbb{C}^{(N-L) \times M}. \end{aligned} \quad (12)$$

Recall that the columns of SVD matrices are ordered by the (real and positive) singular values. These matrices are used to construct the truncated propagator:

$$\mathbf{A}_M := \mathbf{U}_M^H \mathbf{X}_1 \mathbf{V}_M \boldsymbol{\Sigma}_M^{-1} \in \mathbb{C}^{M \times M}. \quad (13)$$

Since exact spectral defectiveness is structurally unstable under finite data and perturbations^{10,11,25}, \mathbf{A}_M generically has a

simple spectrum and admits an eigenvalue decomposition:

$$\mathbf{A}_M = \mathbf{W} \widehat{\boldsymbol{\Lambda}} \mathbf{W}^{-1},$$

where

$$\widehat{\boldsymbol{\Lambda}} = \text{diag}(\widehat{\lambda}_1, \dots, \widehat{\lambda}_M) \in \mathbb{C}^{M \times M},$$

is a diagonal matrix consisting of the eigenvalues $\widehat{\lambda}_j$, and

$$\mathbf{W} = [\mathbf{w}_1 \ \dots \ \mathbf{w}_M] \in \mathbb{C}^{M \times M}$$

is a matrix consisting of the eigenvectors \mathbf{w}_j .

In the DMD literature, there exist two standard methods for mapping a reduced eigenvector $\mathbf{w}_j \in \mathbb{C}^M$ to a *mode* in the signal space \mathbb{C}^{DL} , a mapping commonly referred to as *lifting*.

Projected DMD defines the projected DMD modes using the truncated SVD matrix \mathbf{U}_M as follows:

$$\widehat{\phi}_j^p := \mathbf{U}_M \mathbf{w}_j. \quad (14)$$

By definition, $\widehat{\phi}_j^p \in \mathcal{U}_M$, where \mathcal{U}_M denotes the column space of \mathbf{U}_M :

$$\mathcal{U}_M := \text{col}(\mathbf{U}_M). \quad (15)$$

We note that since $\|\mathbf{w}_j\|_2 = 1$ and \mathbf{U}_M has orthonormal columns, by their construction, projected modes are unit vectors:

$$\|\widehat{\phi}_j^p\|_2 = \|\mathbf{U}_M \mathbf{w}_j\|_2 = 1.$$

Exact DMD uses the (untruncated) snapshot matrix \mathbf{X}_1 and defines the exact DMD modes as follows:

$$\widehat{\phi}_j^e := \mathbf{X}_1 \mathbf{V}_M \boldsymbol{\Sigma}_M^{-1} \mathbf{w}_j. \quad (16)$$

Here, $\widehat{\phi}_j^e \in \text{col}(\mathbf{X}_1)$, implying that the exact DMD modes are not restricted to any subspace of rank M .

Several remarks are due at this point. First, we note that a mode without a superscript, $\widehat{\phi}_j$, may denote either the projected DMD mode $\widehat{\phi}_j^p$ or the exact DMD mode $\widehat{\phi}_j^e$. Therefore, statements written with $\widehat{\phi}_j$ hold for both types.

Second, following the definition of \mathbf{A}_M in (13), the projected and exact modes differ only by projection and scaling, and their explicit relationship is given by

$$\mathbf{P}_{\mathcal{U}_M} \widehat{\phi}_j^e = \widehat{\lambda}_j \widehat{\phi}_j^p, \quad (17)$$

where

$$\mathbf{P}_{\mathcal{U}_M} := \mathbf{U}_M \mathbf{U}_M^H \quad (18)$$

is the orthogonal projector onto \mathcal{U}_M .

Third, in the ideal noiseless case using correct order ($M = m$), the projected DMD and exact DMD coincide: they yield the same eigenvalues and the same modes.

Fourth, we emphasize the distinction between the *underlying signal eigenvalues* $\{\lambda_j\}_{j=1}^m$ and *underlying signal modes*

$\{\phi_j\}_{j=1}^m$ in (6), and the eigenvalues and modes computed by DMD. The latter are estimates of the former. We collect the modes (from either lifting scheme) into a matrix

$$\widehat{\Phi} = [\widehat{\phi}_1 \ \dots \ \widehat{\phi}_M] \in \mathbb{C}^{DL \times M}.$$

The amplitudes $\widehat{\mathbf{b}}$ are determined by enforcing the initial condition, i.e., by solving $\widehat{\Phi}\widehat{\mathbf{b}} \approx \widetilde{\mathbf{x}}_0$. Then, the order- M approximation of the delay-coordinates samples is

$$\widehat{\mathbf{x}}_k = \widehat{\Phi}\widehat{\Lambda}^k\widehat{\mathbf{b}}, \quad k = 0, \dots, N-L. \quad (19)$$

Note that (19) extends naturally to prediction: for any integer $h = 1, 2, \dots$, we have

$$\widehat{\mathbf{x}}_{k+h} = \widehat{\Phi}\widehat{\Lambda}^{k+h}\widehat{\mathbf{b}}, \quad k \geq N-L,$$

where $\widehat{\mathbf{x}}_{k+h}$ is a prediction in the delay-coordinates space. The corresponding prediction in the original signal space is obtained by extracting its first D entries.

C. Signal space, order detection, and component selection

Central to our geometric framework is the *signal subspace*

$$\mathcal{S} := \text{span}\{\phi_1, \dots, \phi_m\}, \quad (20)$$

which contains the spatial structure of the underlying low-dimensional dynamics, where ϕ_1, \dots, ϕ_m are the true underlying signal modes (6). By construction, the noiseless snapshot matrices satisfy

$$\text{col}(\mathcal{S}_0) = \text{col}(\mathcal{S}_1) = \mathcal{S}. \quad (21)$$

We assume that the noise level is sufficiently low such that the span of the principal components of the noisy snapshot matrix \mathcal{U}_M defined in (15) approximately contains the signal subspace \mathcal{S} .

We define $\mathcal{U}_m = \text{col}(\mathcal{U}_m)$, where canonically \mathcal{U}_m contains the leading m left singular vectors, i.e., the m leftmost columns of \mathcal{U}_M . This canonical choice is adopted only for conceptual convenience and has no practical bearing on the developments below. Alternative selections of m vectors from \mathcal{U}_M that optimally approximate the signal subspace are discussed in Appendix B. We make the following quantitative assumption regarding how well \mathcal{U}_m is aligned with the signal subspace \mathcal{S} . We quantify this alignment by the spectral norm of the difference between orthogonal projectors, since it is basis-invariant, and has a direct principal-angle interpretation.

Assumption 2.1 (Signal-subspace proximity). There exists a small $\eta \in [0, 1)$ such that

$$\|\mathcal{P}_{\mathcal{S}} - \mathcal{P}_{\mathcal{U}_m}\|_2 \leq \eta. \quad (22)$$

Since $\dim \mathcal{S} = \dim \mathcal{U}_m = m$, (22) is equivalent to

$$\theta_{\max}(\mathcal{S}, \mathcal{U}_m) \leq \arcsin \eta,$$

where θ_{\max} is the largest principal angle.

Assumption 2.1 formalizes the requirement that, under moderate noise, the m -dimensional truncation subspace \mathcal{U}_m remains sufficiently aligned with the true signal subspace \mathcal{S} , namely,

$$\mathcal{S} \approx \mathcal{U}_m \subseteq \mathcal{U}_M, \quad (23)$$

where “ \approx ” refers to the projector-distance bound (22), and the inclusion holds since \mathcal{U}_m is spanned by a subset of the columns of \mathcal{U}_M . This proximity condition ensures that signal-consistent modes can be distinguished geometrically from spurious components. Heuristically, the approximation of \mathcal{S} by \mathcal{U}_m improves (suggesting the existence of smaller η) with higher Signal-to-Noise Ratio (SNR), better spectral separation, better spatial conditioning, and larger embedding dimension or window length; see Appendix C. In what follows, \mathcal{U}_m serves as an ideal reference subspace, while \mathcal{U}_M provides the practical, data-driven proxy used in mode selection.

In summary, the true order m is unknown, and DMD computed at an overestimated rank $M \geq m$ produces both signal-consistent and spurious components. The central problem is therefore to identify, among the M computed modes, those that are geometrically consistent with the signal subspace. This post hoc formulation provides the structural basis for the mode-selection methods developed in the sequel.

III. RELATED WORK ON ORDER DETECTION AND MODE SELECTION

Existing approaches for order detection and mode selection in DMD can be grouped into four broad families. For comprehensive overviews of DMD variants, selection heuristics, and algorithmic foundations, see^{14,28}.

The first group consists of *spectral and likelihood-based mode selection* methods. Spectral heuristics are widely used for order detection in DMD and for selecting the truncation rank, using gap- or threshold-based rules applied to the singular values of the snapshot matrix^{10,11}. In the context of delay-coordinates, analogous rules are applied to the singular values of the corresponding block-Hankel snapshot matrices²⁶. Eigenvalue screening rules based on magnitude or phase are also commonly employed in practice¹¹. Closely related approaches formulate order detection as penalized likelihood model selection, trading off fit quality with a complexity penalty, for example via Minimum Description Length (MDL) or Bayesian Information Criterion (BIC)^{30–32,37}. Within the DMD framework, likelihood-based selection has been pursued through penalized optimization formulations^{38,39} or Bayesian inference approaches⁴⁰.

The second group comprises *robustness-based mode selection* strategies, which retain components that persist under data resampling, held-out refits, or other perturbations of the snapshots. A prominent example is bagging optimized DMD (BOP-DMD), which fits ensembles across randomized data subsets and selects modes based on their empirical consistency³³. Other stability-based methods assess mode validity using diagnostics such as time-reversal consistency³⁴.

The third group includes *post hoc and structure-aware mode selection* methods, which compute DMD at an over-estimated truncation rank and then perform mode selection in a post-processing step. In contrast to rank estimation or eigenvalue-centric selection methods, some approaches are mode-centric and exploit structural properties of the computed modes. In settings involving delay-coordinates, representative examples test for KV structure across delays in the resulting delay-coordinates modes²⁹. Related post-processing strategies have also been developed in closely connected subspace and matrix-pencil settings^{41,42}. A complementary post hoc direction uses *residual-based verification* to filter or rank eigenpairs by numerical consistency, aiming to mitigate spectral pollution; while this provides an eigenpair-level diagnostic, it does not consider the organization of modes induced by delay-coordinates⁴³.

The fourth group consists of *energy- and amplitude-based heuristics*, which rank modes by simple magnitude proxies such as Euclidean norms or reconstruction amplitudes^{1,10}. These should be understood as practical magnitude proxies, rather than as likelihood- or energy-based models. These heuristics are appealing due to their simplicity and low computational cost. However, norms and amplitudes depend on algorithmic choices and can be sensitive to noise.

The above approaches address order detection and mode selection from complementary perspectives, but important gaps remain. Spectral heuristics rely on global summaries and degrade under noise, spectral crowding, or damping. Information-criterion methods require refitting models across hypothesized orders, making them computationally expensive and sensitive to noise-model mismatch. Robustness-based approaches emphasize empirical stability but do not provide a structural interpretation of the recovered components or a principled definition of true versus spurious modes. Norm- and amplitude-based heuristics are simple to apply but can become unreliable in delay-coordinates settings and lack a clear mechanistic justification. Structure-aware post hoc methods explicitly formalize the expected organization of *true* modes arising from delay-coordinates, but the corresponding geometric characterization of *spurious* modes remains largely implicit. Spurious components are typically treated as unstructured residual artifacts rather than as objects with their own systematic geometry. As a result, existing methods do not exploit the subspace and structural organization of spurious modes in their selection rules, leaving the geometric distinction between true and spurious components under delay-coordinates insufficiently understood.

IV. MODE GEOMETRY, SIGNAL SUBSPACE RESIDUAL, AND TRUE AND SPURIOUS MODES

This section presents a geometric analysis of the DMD modes and, based on it, derives a practical method for mode selection.

By definition (20), the signal subspace \mathcal{S} spans the m underlying signal modes $\{\phi_j\}_{j=1}^m$ (6). However, in practice, m is unknown and the underlying signal modes are accessed only

through the $M > m$ computed DMD modes $\{\hat{\phi}_j\}_{j=1}^M$. We now define a partition of the computed DMD modes into *true* and *spurious* modes, where the true modes can be viewed as noisy estimators of the underlying signal modes.

Definition 4.1 (Signal-subspace residual vector). For any vector $v \in \mathbb{C}^{DL}$, the Signal-Subspace Residual (SSR) vector is defined by

$$r_{\mathcal{S}}(v) := (I - P_{\mathcal{S}})v, \quad (24)$$

where $P_{\mathcal{S}}$ is the orthogonal projector onto the signal subspace \mathcal{S} .

We define the *true* modes to be the m modes with the smallest residual norms, and the remaining $M - m$ modes to be *spurious*.

Definition 4.2 (True and spurious modes). Given M computed modes $\{\hat{\phi}_j\}_{j=1}^M$ (either exact or projected), let $\mathcal{J}_{\text{true}} \subset \{1, \dots, M\}$ be a set of m indices attaining the m smallest values of

$$\|r_{\mathcal{S}}(\hat{\phi}_j)\|_2^2, \quad j = 1, \dots, M,$$

and let $\mathcal{J}_{\text{spur}} := \{1, \dots, M\} \setminus \mathcal{J}_{\text{true}}$. For each $j \in \{1, \dots, M\}$, $\hat{\phi}_j$ is a *true mode* if $j \in \mathcal{J}_{\text{true}}$, and a *spurious mode* otherwise.

Definition 4.2 suggests that the modes can be classified as true or spurious by evaluating their residual energy outside the signal subspace \mathcal{S} . However, since \mathcal{S} cannot be directly observed, this definition serves only as an ideal reference for distinguishing between true and spurious modes. To bridge this gap, we introduce a practical criterion for differentiating true and spurious DMD modes.

By Assumption 2.1, the m -dimensional subspace \mathcal{U}_m is close to \mathcal{S} . However, the true order m , and therefore \mathcal{U}_m , are unknown. We postulate that \mathcal{U}_M , where $M > m$ is an arbitrary overestimate of the true order, can serve as a practical proxy for \mathcal{S} . We therefore propose to measure residual energy with respect to \mathcal{U}_M rather than \mathcal{S} , using the orthogonal projector $P_{\mathcal{U}_M}$.

Definition 4.3 (Estimated-subspace residual vector). For an exact DMD mode $\hat{\phi}_j^e$, define the Estimated-Subspace Residual (ESR) vector by

$$r_{\mathcal{U}_M}(\hat{\phi}_j^e) := (I - P_{\mathcal{U}_M})\hat{\phi}_j^e, \quad j = 1, \dots, M. \quad (25)$$

We note that Definition 4.3 is only informative for exact DMD modes because the projected modes lie in \mathcal{U}_M by construction, and so their residual is $r_{\mathcal{U}_M}(\hat{\phi}_j^p) \equiv 0$.

Figure 1 summarizes the geometry of the SSR and the ESR and highlights that ESR captures the \mathcal{U}_M^\perp component of SSR.

We propose to estimate the partition of modes into true and spurious based on the squared norm of the ESR vectors:

$$\mathcal{R}_j := \|r_{\mathcal{U}_M}(\hat{\phi}_j^e)\|_2^2. \quad (26)$$

Specifically, the scores in logarithmic scale $\zeta_j := \log(\mathcal{R}_j + \varepsilon)$ for some small $\varepsilon > 0$, are clustered into two groups, and the

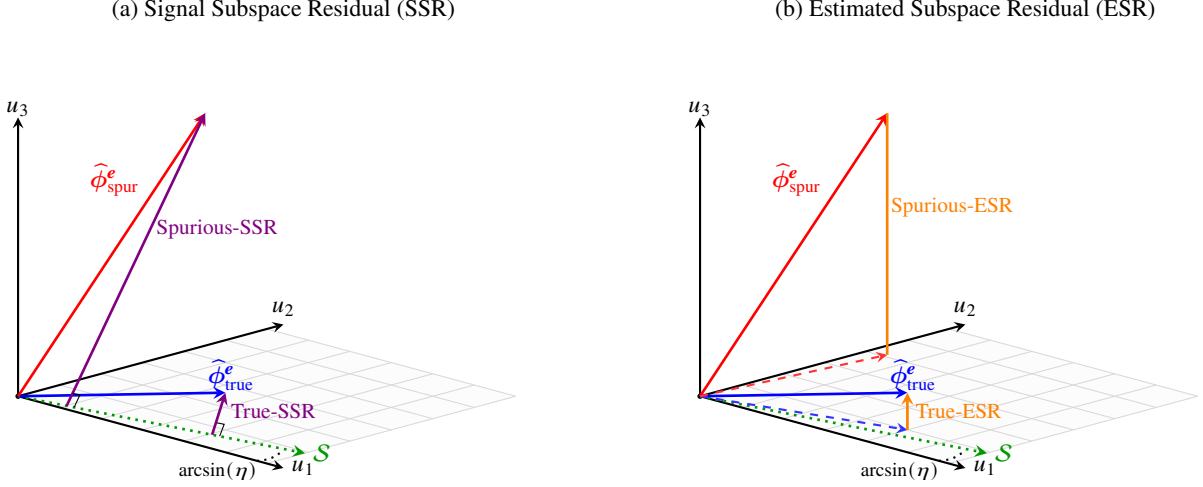


FIG. 1. Geometric illustration of signal-subspace residual (SSR) and estimated-subspace residual (ESR) in the case $m = 1$ and $M = 2$, where the true signal subspace \mathcal{S} (green) lies inside the truncation subspace $\mathcal{U}_M = \text{span}\{u_1, u_2\}$. True and spurious modes are drawn in blue and red, respectively, together with their projections onto \mathcal{U}_M (dashed). (a) SSR corresponds to the in-plane deviation of a mode from \mathcal{S} , shown as violet arrows. (b) ESR corresponds to the out-of-plane component of a mode, shown as orange arrows. In this constructed example, the true mode has small SSR and ESR, whereas the spurious mode has larger residual in both senses.

cluster with the smaller values ζ_j is labeled *true*. Algorithm 1 summarizes this procedure.

In Section VII, we empirically show that Algorithm 1 reliably separates true and spurious modes and outperforms standard baselines. The intuition behind the separating power based on the norms of the ESR vectors is as follows; If $\hat{\phi}_j^e$ is a true mode, it is dominated by the signal component, so its energy concentrates on the signal subspace \mathcal{S} and therefore, by Assumption 2.1, on \mathcal{U}_m . Since $\mathcal{U}_m \subset \mathcal{U}_M$, a true mode typically places very little energy outside \mathcal{U}_M (and hence in \mathcal{U}_M^\perp), so $\|\mathbf{r}_{\mathcal{U}_M}(\hat{\phi}_j^e)\|_2^2$ is small.

Conversely, if $\hat{\phi}_j^e$ is a spurious mode, it is a noise-driven artifact of the finite-rank least-squares fit rather than of coherent low-dimensional structure in the data. Such modes are not associated with the signal subspace and therefore are not confined to any low-dimensional subspace, typically placing non-negligible energy outside \mathcal{U}_M . This behavior is consistent with well-documented observations of spectral pollution and noise-induced modes in practical DMD computations^{28,44}. Consequently, a spurious mode generally has a larger component in \mathcal{U}_M^\perp , and thus $\|\mathbf{r}_{\mathcal{U}_M}(\hat{\phi}_j^e)\|_2^2$ is large relative to that of a true mode.

To compute the residual norm efficiently, following (17), we decompose the exact mode as

$$\hat{\phi}_j^e = \hat{\lambda}_j \hat{\phi}_j^p + \mathbf{r}_{\mathcal{U}_M}(\hat{\phi}_j^e). \quad (27)$$

Since $\|\hat{\phi}_j^p\|_2 = 1$ and $\mathbf{r}_{\mathcal{U}_M}(\hat{\phi}_j^e) \in \mathcal{U}_M^\perp$, the two terms in (27) are orthogonal, and hence

$$\|\hat{\phi}_j^e\|_2^2 = |\hat{\lambda}_j|^2 + \|\mathbf{r}_{\mathcal{U}_M}(\hat{\phi}_j^e)\|_2^2. \quad (28)$$

Therefore,

$$\|\mathbf{r}_{\mathcal{U}_M}(\hat{\phi}_j^e)\|_2^2 = \|\hat{\phi}_j^e\|_2^2 - |\hat{\lambda}_j|^2. \quad (29)$$

Require: Eigenpairs $\{(\hat{\lambda}_j, \hat{\phi}_j^e)\}_{j=1}^M$, small $\varepsilon > 0$; clustering routine and aggregate as in Algorithm 2
Ensure: Order estimate \hat{m} and labels $\{\ell_j\}$

- 1: **for** $j = 1, \dots, M$ **do**
- 2: $\mathcal{R}_j \leftarrow \|\hat{\phi}_j^e\|_2^2 - |\hat{\lambda}_j|^2$ ▷ by (29)
- 3: $\zeta_j \leftarrow \log(\mathcal{R}_j + \varepsilon)$
- 4: **end for**
- 5: Form score vector $\mathbf{f} = (\zeta_1, \dots, \zeta_M)^\top$
- 6: Apply binary mode selection framework (Algorithm 2) to \mathbf{f} to obtain labels $\{\ell_j\}$ and \hat{m}

Algorithm 1. Mode selection based on the norms of the residual vectors.

The expression in (29) implies that the residual norms can be computed directly from the norms of the exact modes and the magnitudes of the eigenvalues, without forming $\mathbf{P}_{\mathcal{U}_M}$. This adds only a negligible additional cost beyond the cost of SVD used in the standard delay-coordinates DMD. For a complete complexity analysis, see Appendix G.

We end this section with a few remarks. First, we note that the clustering step in Algorithm 1 is generic and can be used with any per-mode scalar score. In particular, one may pass $f_j = \log(\mathcal{R}_j + \varepsilon)$ (or any other appropriate scaling) into the framework in Algorithm 2. We found empirically that the residual scores \mathcal{R}_j typically exhibit a clear separation between small and large values under moderate noise, and logarithmic scaling improves numerical stability by compressing the dynamic range prior to clustering.

Second, since the scores \mathcal{R}_j can be computed directly from the rank- M DMD eigenpairs via (29), the mode selection in Algorithm 1 applies to the classical case, where $L = 1$ without delay-coordinates.

Require: Score vector $\mathbf{f} = (f_1, \dots, f_M)^\top \in \mathbb{R}^M$ (smaller is better), clustering routine with $k = 2$ (e.g., K-Means, GMM), aggregate agg (default: mean)

Ensure: Labels $\ell_j \in \{\text{true, spurious}\}$ and order estimate \hat{m}

- 1: (optional) Normalize \mathbf{f} (e.g., affine rescaling)
- 2: $\{C_1, C_2\} \leftarrow \text{CLUSTER}(\mathbf{f}, k = 2)$
- 3: $C_{\text{true}} \leftarrow \arg \min_{C \in \{C_1, C_2\}} \text{agg}(\{f_j\}_{j \in C})$
- 4: **for** $j = 1, \dots, M$ **do**
- 5: $\ell_j \leftarrow \text{true}$ if $j \in C_{\text{true}}$ else $\ell_j \leftarrow \text{spurious}$
- 6: **end for**
- 7: $\hat{m} \leftarrow |C_{\text{true}}|$

Algorithm 2. Binary mode selection framework

V. KRONECKER-VANDERMONDE STRUCTURE IN MODES

Assuming an exponential signal model as in (6), Bronstein *et al.*²⁹ showed that, when using delay-coordinates, each true mode exhibits a KV structure of the form

$$\mathbf{v}_L(\lambda_j) \otimes \phi_j = \begin{bmatrix} \phi_j \\ \lambda_j \phi_j \\ \vdots \\ \lambda_j^{L-1} \phi_j \end{bmatrix} \in \mathbb{C}^{DL}, \quad (30)$$

where $\mathbf{v}_L(\lambda) \in \mathbb{C}^L$ is the Vandermonde vector:

$$\mathbf{v}_L(\lambda) = [1, \lambda, \dots, \lambda^{L-1}]^\top, \quad (31)$$

and \otimes is the Kronecker product, defined by

$$\mathbf{a} \otimes \mathbf{b} := \begin{bmatrix} a_1 \mathbf{b} \\ a_2 \mathbf{b} \\ \vdots \\ a_L \mathbf{b} \end{bmatrix} \in \mathbb{C}^{DL}. \quad (32)$$

for any $\mathbf{a} \in \mathbb{C}^L$ and $\mathbf{b} \in \mathbb{C}^D$. See App. D for a compact derivation of this result. Here, we extend this analysis in three ways. First, we derive the same KV structure without assuming a signal model, showing that this structure is induced by the delay-coordinates rather than by the signal model. Second, our new derivation shows that KV structure can arise in both *true* and *spurious* components, often with different strengths (with true modes adhering significantly more strongly). This motivates continuous KV-deviation metrics that quantify the extent to which each mode conforms to the KV template, while avoiding undue sensitivity to small, localized perturbations. Third, we link the new derivation of the KV structure to the ESR (Definition 4.3) and use their relationship to devise a new mode-selection algorithm, complementary to Algorithm 1, which is based on the ESR, and to the algorithm proposed in Ref. 29.

We note that this KV structure implies that, in delay-coordinates, a mode no longer represents a purely spatial pattern in \mathbb{C}^D , but rather a coupled spatiotemporal pattern in \mathbb{C}^{DL} : its D -dimensional lagged segments are tied across lags by a geometric progression parameterized by λ_j . This structure is illustrated schematically in Fig. 2.

A. Block-companion minimizer and compression

To derive the KV structure without assuming a particular signal model, we examine the following unconstrained least-squares problem:

$$\min_{\mathbf{A} \in \mathbb{C}^{DL \times DL}} \|\mathbf{X}_1 - \mathbf{A}\mathbf{X}_0\|_F^2, \quad (33)$$

where $\mathbf{X}_0, \mathbf{X}_1 \in \mathbb{C}^{DL \times N}$ are the snapshot matrices defined in (9). Although the minimizer of (33) is not necessarily unique, there exists a minimizer whose structure is dictated by the delay-coordinates.

Lemma 5.1 (Block-companion minimizer). *The optimization problem (33) admits the minimizer C_L with the following block-companion form:*

$$C_L = \begin{bmatrix} \mathbf{0} & I_D & & \mathbf{0} \\ & \ddots & \ddots & \\ & & \mathbf{0} & I_D & \mathbf{0} \\ B_1 & B_2 & \cdots & B_{L-1} & B_L \end{bmatrix} \in \mathbb{C}^{DL \times DL}, \quad (34)$$

where $B_\ell \in \mathbb{C}^{D \times D}$.

Proof See Appendix E 1.

Lemma 5.1 shows that the delay-coordinates are explicitly encoded in a minimizer: the top $L - 1$ block rows implement the one-step shift between consecutive delay blocks, while the last block row defines a linear predictor of the next sample from the stacked history $\tilde{\mathbf{x}}_k = [\mathbf{x}_k^\top, \dots, \mathbf{x}_{k+L-1}^\top]^\top$, namely $\mathbf{x}_{k+L} \approx \mathbf{B} \tilde{\mathbf{x}}_k$, where $\mathbf{B} = [B_1 \cdots B_L] \in \mathbb{C}^{D \times DL}$. Throughout, we fix C_L by taking \mathbf{B} to be the Moore-Penrose (pseudoinverse) least-squares predictor; Appendix E 1 makes this choice explicit.

Lemma 5.2 (Eigenvectors of block-companion matrices (see, e.g., Ref. 45)). *Any eigenvector of C_L associated with eigenvalue $\mu \in \mathbb{C}$ has the following Kronecker-Vandermonde form:*

$$\mathbf{v}_L(\mu) \otimes \varphi, \quad (35)$$

where $\mathbf{v}_L(\mu) = [1, \mu, \dots, \mu^{L-1}]^\top$, and $\varphi \in \mathbb{C}^D \setminus \{\mathbf{0}\}$.

Proof. See Appendix E 2.

We now connect the block-companion solution $C_L \in \mathbb{C}^{DL \times DL}$ of (34) to the truncated DMD propagator $\mathbf{A}_M \in \mathbb{C}^{M \times M}$ defined in (13).

Proposition 5.3. *The truncated DMD propagator can be recast as*

$$\mathbf{A}_M = \mathbf{U}_M^H C_L \mathbf{U}_M, \quad (36)$$

where \mathbf{U}_M is defined in (12).

Proof. See Appendix E 4.

Based on Proposition 5.3, we connect the eigenvectors of C_L , which have a KV structure (Lemma 5.2), to the projected-DMD modes.

Theorem 5.4. Let $(\hat{\lambda}_j, w_j)$ be an eigenpair of the reduced propagator \mathbf{A}_M defined in (13), and let $\hat{\phi}_j^p$ and $\hat{\phi}_j^e$ be the associated projected and exact DMD modes defined in (14) and (16), respectively. Then, $(\hat{\lambda}_j, \hat{\phi}_j^p)$ satisfies

$$(\mathbf{C}_L - \hat{\lambda}_j \mathbf{I}) \hat{\phi}_j^p = r_{u_M}(\hat{\phi}_j^e), \quad (37)$$

where $r_{u_M}(\hat{\phi}_j^e)$ is the corresponding estimated-subspace residual vector (Definition 4.3).

Proof. See Appendix E5. Theorem 5.4 shows that the estimated subspace residual vector $r_{u_M}(\hat{\phi}_j^e)$ governs (through the spectrum of \mathbf{C}_L) the extent to which the projected mode $\hat{\phi}_j^p$ conforms to the KV structure exhibited by the eigenvectors of the block-companion minimizer \mathbf{C}_L . In particular, $r_{u_M}(\hat{\phi}_j^e) = \mathbf{0}$ implies that $\hat{\phi}_j^p$ is an eigenvector of \mathbf{C}_L , and hence has exact Kronecker–Vandermonde structure. Specifically, $r_{u_M}(\hat{\phi}_j^e)$ is exactly the eigenrelation residual of the projected eigenpair $(\hat{\lambda}_j, \hat{\phi}_j^p)$ with respect to \mathbf{C}_L .

Theorem 5.4 therefore provides a structural link that motivates KV-deviation metrics as a complementary criterion: the ESR norm $\|r_{u_M}(\hat{\phi}_j^e)\|_2$ directly measures the extent to which the projected DMD mode violates the companion eigenrelation. Since the eigenvectors of \mathbf{C}_L have KV structure, smaller ESR suggests closer KV consistency, while larger ESR indicates a stronger departure from the ideal KV form. In Sec. IV, the ESR norm was used to separate true and spurious components; the link established here motivates KV deviation as an additional structural score for mode selection.

B. Nested DMD

Above, we showed that delay-embedded DMD induces KV structure in the computed modes. We postulate that true modes adhere more closely to the KV template than spurious modes. We therefore introduce direct KV-deviation scores computed from the mode entries and $\hat{\lambda}_j$, and use them as structural features for separating true and spurious modes.

Here, we propose a different, direct quantification of the deviation of each mode from the KV structure, and then, use this deviation as a feature for separating true from spurious modes.

To motivate the proposed quantification, consider the *ideal KV template* for a projected DMD mode:

$$\hat{\phi}_j^p = \mathbf{v}_L(\hat{\lambda}_j) \otimes \hat{\phi}_j^{(0)}, \quad \hat{\phi}_j^{(0)} \in \mathbb{C}^D, \quad (38)$$

where $\mathbf{v}_L(\lambda) := [1, \lambda, \dots, \lambda^{L-1}]^\top$. Reshaping this mode, of length DL , as a $D \times L$ matrix by organizing blocks of D coordinates as L columns, yields

$$[\hat{\phi}_j^{(0)}, \hat{\lambda}_j \hat{\phi}_j^{(0)}, \dots, \hat{\lambda}_j^{L-1} \hat{\phi}_j^{(0)}]. \quad (39)$$

Viewing this matrix as a sequence of columns, the ℓ th column can be recast as

$$\tilde{b}_j \tilde{\phi}_j \hat{\lambda}_j^\ell, \quad (40)$$

where $\tilde{b}_j := \|\hat{\phi}_j^{(0)}\|_2$ and $\tilde{\phi}_j := \hat{\phi}_j^{(0)} / \|\hat{\phi}_j^{(0)}\|_2$. This expression coincides with the one-mode specialization of (6), with the lag index ℓ replacing the time index k . Therefore, this reshaped form is consistent with the signal model assumed by an order-1 DMD.

Consequently, we reshape each computed projected mode $\hat{\phi}_j^p = [\hat{\phi}_j^{(0)}; \dots; \hat{\phi}_j^{(L-1)}]$ as above, obtaining the following mode matrix,

$$\hat{\mathbf{\Phi}}_j := [\hat{\phi}_j^{(0)}, \dots, \hat{\phi}_j^{(L-1)}] \in \mathbb{C}^{D \times L}. \quad (41)$$

Then, we apply an order-1 DMD to the column sequence of $\hat{\mathbf{\Phi}}_j$, along the lag axis, yielding a single DMD eigenvalue $\tilde{\lambda}_j \in \mathbb{C}$ and a corresponding DMD mode $\tilde{\phi}_j^{(0)} \in \mathbb{C}^D$.

Following the standard DMD reconstruction convention, we reconstruct the rank-1 mode matrix by:

$$\hat{\mathbf{\Phi}}_j^{(\text{KV})} := (\tilde{\phi}_j^{(0)} \tilde{\phi}_j^{(0)H} \hat{\phi}_j^{(0)}) \mathbf{v}_L^\top(\tilde{\lambda}_j), \quad (42)$$

where $\hat{\phi}_j^{(0)}$ is the first column of $\hat{\mathbf{\Phi}}_j$.

Based on the reconstructed matrix $\hat{\mathbf{\Phi}}_j^{(\text{KV})}$, we define a KV-deviation score as the mean squared reconstruction error:

$$\mathcal{R}_j^{(\text{KV})} := \frac{\|\hat{\mathbf{\Phi}}_j - \hat{\mathbf{\Phi}}_j^{(\text{KV})}\|_F^2}{DL}. \quad (43)$$

The score $\mathcal{R}_j^{(\text{KV})}$ is a direct KV-deviation metric: it vanishes when the reshaped mode follows an exact rank-1 KV template along the lag axis and increases as the mode departs from KV structure.

From this point onward we follow Algorithm 1: we apply the same score scaling and then the binary mode selection framework (Algorithm 2). Here the per-mode feature is scalar and derived from $\mathcal{R}_j^{(\text{KV})}$. Algorithm 3 summarizes this procedure.

Require: Projected modes $\{\hat{\phi}_j^p\}_{j=1}^M \subset \mathbb{C}^{DL}$, embedding length L , spatial dimension D , small $\varepsilon > 0$; clustering routine and aggregation rule as in Algorithm 2

Ensure: Order estimate \hat{m} and labels $\{\ell_j\}_{j=1}^M$

- 1: **for** $j = 1, \dots, M$ **do**
- 2: $\hat{\mathbf{\Phi}}_j \leftarrow$ reshape($\hat{\phi}_j^p$, $D \times L$)
- 3: Run rank-1 DMD on $\hat{\mathbf{\Phi}}_j$ to obtain $(\tilde{\phi}_j^{(0)}, \tilde{\lambda}_j)$
- 4: $\mathbf{y}_0 \leftarrow$ first column of $\hat{\mathbf{\Phi}}_j$
- 5: $\hat{\mathbf{\Phi}}_j^{(\text{KV})} \leftarrow (\tilde{\phi}_j^{(0)} \tilde{\phi}_j^{(0)H} \mathbf{y}_0) \mathbf{v}_L(\tilde{\lambda}_j)^\top$
- 6: $\mathcal{R}_j^{(\text{KV})} \leftarrow \|\hat{\mathbf{\Phi}}_j - \hat{\mathbf{\Phi}}_j^{(\text{KV})}\|_F^2 / (DL)$
- 7: $\zeta_j \leftarrow \log(\mathcal{R}_j^{(\text{KV})} + \varepsilon)$
- 8: **end for**
- 9: Stack features $\zeta \leftarrow [\zeta_1, \dots, \zeta_M]$
- 10: Apply binary mode selection framework (Algorithm 2) to ζ to obtain labels $\{\ell_j\}$ and \hat{m}

Algorithm 3. KV deviation via nested rank-1 DMD (binary mode selection framework)

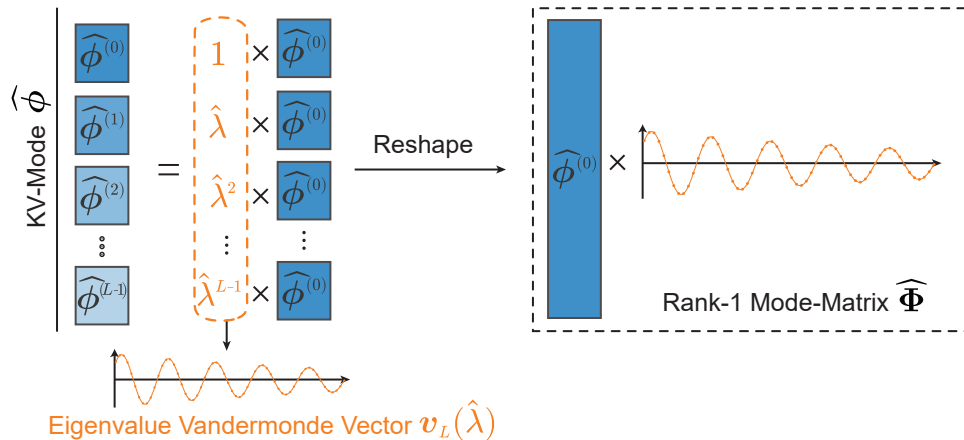


FIG. 2. Kronecker–Vandermonde structure of a DMD mode. A KV mode is formed by stacking L lag segments of length D , where each segment is a scaled and rotated copy of a base spatial vector $\widehat{\phi}^{(0)}$. The multipliers $\widehat{\lambda}^\ell$ form the Vandermonde vector $\mathbf{v}_L(\widehat{\lambda}) = [1, \widehat{\lambda}, \dots, \widehat{\lambda}^{L-1}]^\top$, illustrated at the bottom. Reshaping the KV mode yields the rank-1 outer product $\widehat{\phi}^{(0)} \mathbf{v}_L(\widehat{\lambda})^\top$, mirroring the rank-1 structure underlying order-1 DMD.

The nested rank-1 construction replaces one delay-coordinates DMD fit of unknown order with M independent order-1 fits along the lag axis, one per mode.

The added cost scales linearly with D , L , and M and is negligible compared with the truncated SVD used to form the projected modes; see Appendix G for detailed asymptotic costs.

As a simpler variant, we consider a *fixed-eigenvalue KV fit* (FEKVF). Here “fixed eigenvalue” means that we do not re-estimate a lag-axis eigenvalue: we set the lag multiplier to the original DMD eigenvalue $\widehat{\lambda}_j$ and fit only the spatial coefficient in the KV template. For each mode this amounts to the least-squares problem

$$\min_{\varphi \in \mathbb{C}^D} \|\widehat{\Phi}_j - \varphi \mathbf{v}_L(\widehat{\lambda}_j)^\top\|_F^2,$$

yielding a single scalar deviation score in closed form (Appendix F). Compared with the nested rank-1 method, FEKVF removes the inner order-1 DMD step and is therefore computationally cheaper per mode.

VI. CONNECTION TO EXISTING ORDER DETECTION METHODS

This section interprets existing order detection heuristics through the geometric framework developed above. In particular, we show that commonly used magnitude-based ranking rules implicitly conflate eigenvalue scaling with subspace residual geometry, and therefore degrade under delay-coordinates.

A. Spatiotemporal coupling ratio-based method

Both the approach of Bronstein *et al.*²⁹ and our approach use KV structure to form per-mode scores that are small when the structure is present. Bronstein *et al.*²⁹ do so via entrywise quotient checks across consecutive lag blocks, testing whether $(\widehat{\phi}_j^{(\ell+1)})_d / (\widehat{\phi}_j^{(\ell)})_d \approx \widehat{\lambda}_j$ for entries d within each block, and aggregating the results. In delay-coordinates, however, ratio tests can be numerically fragile: whenever $(\widehat{\phi}_j^{(\ell)})_d$ is small, the quotient is ill-conditioned and can take arbitrarily large values, so the aggregate can be dominated by a few unstable coordinates. Our analysis suggests that KV adherence is a continuous property shared by true and spurious modes to different degrees, so quotient checks often behave like a near-binary test (pass or fail). In contrast, our KV-fit score measures a graded distance from the KV template through a global reconstruction error. We compare these criteria numerically in Sec. VII.

B. Mode-norm

A common order-detection method in standard DMD ranks modes by the Euclidean norm of the exact-DMD mode, $\|\widehat{\phi}_j^\epsilon\|_2$, motivated by the intuition that true modes carry larger energy than spurious modes. Our analysis in Sec. IV sheds new light on this heuristic. In (28), the squared-norm of exact DMD modes $\|\widehat{\phi}_j^\epsilon\|_2^2$ is expressed as the sum of the squared magnitude of the eigenvalue $|\widehat{\lambda}_j|^2$ and the ESR squared-norm $\|r_{u_M}(\widehat{\phi}_j^\epsilon)\|_2^2$.

When using delay-coordinates, we empirically observe that the magnitude of the eigenvalue loses its discriminative power.

Specifically, as the embedding length L grows, the bulk of spurious eigenvalue magnitudes concentrates in an annular band near the unit circle, as illustrated in Fig. 3 (left panel). Intuitively, delay embedding enlarges the lifted state dimension while preserving the shift structure of the block-companion operator, increasing the effective polynomial degree governing spurious components. This induces a magnitude concentration near the unit circle, reducing the discriminative power of eigenvalue magnitude alone. This behavior is qualitatively consistent with annulus concentration phenomena studied for random polynomial roots; see Soundararajan⁴⁶ for a detailed analysis.

We first focus on the case where L is sufficiently large, so that spurious modes satisfy $|\widehat{\lambda}_j| \approx 1$ for $j \in \mathcal{J}_{\text{spur}}$.

In the weakly damped case, the underlying eigenvalues satisfy $|\widehat{\lambda}_j| \approx 1$, for $j \in [m]$, where we assume that the associated DMD eigenvalues satisfy $|\widehat{\lambda}_j| \approx |\lambda_j|$ for $j \in \mathcal{J}_{\text{true}}$ to simplify the discussion. In this case, both true and spurious eigenvalues cluster near the unit circle as L increases. Consequently, eigenvalue magnitude becomes nearly independent of mode identity, and, by the decomposition of the exact DMD mode squared norm in (28), the only discriminative component of the exact-mode norm is the ESR squared norm $|\mathbf{r}_{\mathcal{U}_M}(\widehat{\phi}_j^e)|_2^2$. Using the mode norm $\|\widehat{\phi}_j^e\|_2^2$ therefore confounds this informative ESR norm with the non-informative eigenvalue magnitude $|\widehat{\lambda}_j|^2$. Since the eigenvalue magnitudes may vary independently of mode identity, they mask or dilute the separation between true and spurious modes. For this reason, it is preferable to work directly with the ESR norm, which isolates the meaningful geometric information without contamination from eigenvalue scaling.

Next, consider a strongly damped signal, where the underlying eigenvalues satisfy $|\lambda_j| < 1$ for $j \in [m]$. When L is sufficiently large, spurious modes typically have $|\widehat{\lambda}_j| \approx 1$, while true DMD modes have smaller $|\widehat{\lambda}_j|$. In addition, true modes typically have smaller ESR energies than spurious modes. Together, these two facts imply that true modes tend to have *smaller* exact-mode norms than spurious modes. This is the opposite of how the heuristic is commonly applied, which treats larger norms as more likely to be true.

For completeness, we note that for small- L embeddings (and in the standard DMD case $L = 1$), spurious eigenvalues are often observed well inside the unit disk. In this regime, true modes typically have significantly larger $|\widehat{\lambda}_j|^2$ than spurious modes, so mode-norm ranking *is* an effective separator. However, the ESR norm contributes in the opposite direction, being larger for spurious modes, and therefore it weakens the separation provided by $|\widehat{\lambda}_j|^2$ alone. The numerical evaluation in Sec. VII compares mode-norm ranking with a detector based purely on $|\widehat{\lambda}_j|$ for $L = 1$.

These observations illustrate that eigenvalue magnitude and mode norm are not intrinsic indicators of dynamical relevance under delay embedding, whereas the ESR isolates the geometric quantity that directly reflects signal-subspace consistency and mode identity.

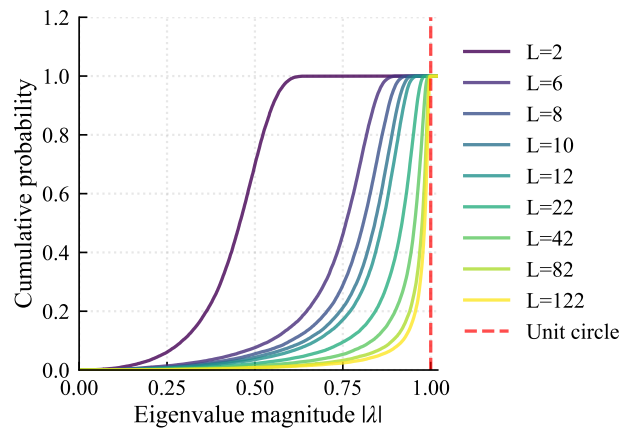


FIG. 3. Spurious eigenvalue magnitude statistics versus embedding length L . For each L , we pool the magnitudes $|\widehat{\lambda}|$ of all spurious eigenvalues from all Monte–Carlo trials and plot the resulting empirical CDF (one curve per L). Overall, spurious eigenvalue magnitudes shift upward with increasing L , but the pooled distributions retain a non-negligible lower tail.

VII. NUMERICAL RESULTS

This section presents results of numerical experiments. We first evaluate the performance of our proposed order-detection methods and compare them with existing baselines. We then report experiments that illustrate the spurious-eigenvalue magnitude behavior discussed in Sec. VI B.

A. Experimental setup

We simulate signals according to eq. (1) using the linear m -mode signal described in (7), with additive Gaussian noise. (We note that we observed qualitatively similar performance under other noise distributions, including bi-Gaussian, heavy-tailed Student’s t , uniform, and heteroscedastic noise, but report only Gaussian results here for brevity.) The ground-truth spatial modes ϕ_j are drawn independently and normalized to unit norm.

Across experiments, we control the following generation parameters: the SNR, the number of true modes m , the eigenvalue magnitudes (we use a common value by setting $\rho_j = \rho$ for all j so that damping is controlled by the single scalar ρ), the minimal phase gap $\Delta\theta$, and the amplitude heterogeneity κ_b . The minimal phase gap is defined as

$$\Delta\theta = \min_{j \neq k} \min(|\theta_j - \theta_k|, 2\pi - |\theta_j - \theta_k|). \quad (44)$$

Amplitude heterogeneity is quantified by

$$\kappa_b = \frac{\max_j |b_j|}{\min_j |b_j|}. \quad (45)$$

B. Order Detection Evaluations

We compare our methods (ESR-energy, KV deviation via nested rank-1 DMD, and fixed-eigenvalue KV fit) with the baselines BIC, Spectral Gap (GAP), and Spatiotemporal Consistency (STC) from Section III. Performance is measured by the order-hit probability, defined as the fraction of trials in which the estimated order equals the actual order m , across 500 trials.

In each experiment, we vary a single parameter (SNR, spectral separation, damping, amplitude heterogeneity) while keeping all other quantities at fixed working-point values.

Fig. 4, shows the order-hit probability as a function of SNR under Gaussian noise. Our methods outperform all three baselines across the entire test range. As SNR increases, all methods exhibit a transition region where hit probability rises from near zero to near one. The KV-deviation methods reach this transition at the lowest SNR, followed closely by ESR-energy. BIC shows a similar pattern but with a later transition. STC and GAP increase more gradually and do not approach perfect accuracy. Increasing the number of modes, m , shifts all transitions toward higher SNR values with the same ordering among methods.

Fig. 5 presents the order-hit probability as a function of the minimal phase separation $\Delta\theta$ under Gaussian noise. Across the tested range, our methods consistently achieve higher hit probabilities than all three baselines. As $\Delta\theta$ increases, all methods move from near-zero to near-one hit probability, with the KV-deviation criteria transitioning at the smallest gaps and ESR-energy close behind. BIC follows the same pattern but becomes reliable only at larger separations, GAP requires substantially wider gaps before saturating, and STC increases more slowly and reaches only moderate accuracy. Again, increasing m shifts the transition regions toward larger phase gaps while leaving the relative ordering of methods unchanged.

Fig. 6 shows the order-hit probability as a function of the common magnitude ρ under Gaussian noise. Throughout the tested range, our methods consistently outperform the baselines, achieving higher hit probabilities for all values of ρ . As ρ increases toward one, all methods improve, but the same performance hierarchy persists: the KV-deviation scores become reliable at the smallest damping, ESR-energy follows closely, and BIC only catches up at larger values of ρ . GAP eventually attains high accuracy but only when ρ is very close to one. In contrast to the phase-separation experiment, STC does not saturate within the tested range and instead increases slowly and approximately monotonically. As before, increasing m shifts the transition regions toward larger ρ while leaving the ordering among methods unchanged.

Figure 7 shows the order-hit probability as a function of amplitude heterogeneity κ_b under Gaussian noise. Across the tested range, our methods consistently outperform the baselines, maintaining substantially higher hit probabilities as the amplitudes become more uneven. As κ_b increases, the baseline methods (STC, BIC, GAP) deteriorate sharply and their hit probabilities collapse over most of the range. In contrast, the KV-deviation methods and ESR-energy remain stable and accurate, with only a modest decline in the most heterogeneous

regime and only for $m = 5$.

To summarize the one-dimensional sweeps in Figs. 4–7, Table I reports normalized AUC values aggregated over each sweep.

Figure 8 shows the order-hit probability as a function of the complexity of the underlying signal, quantified by the number of true modes m . Our methods remain detailed and robust until a collapse point determined by the signal parameters (dimensions, SNR, etc.), here observed at $m = 15$. In contrast, the performance of the baseline methods collapses much earlier. BIC is particularly sensitive to the model order, failing almost completely for $m > 3$. STC and GAP also degrade significantly, while ESR-energy and the KV-deviation methods remains robust for a wider range of m .

Fig. 9 presents the hit probability in the absence of delay-coordinates, i.e., $L = 1$. To satisfy the inequality $DL < N - L$, we set $D = 220$ while keeping the other parameters fixed. We compare the performance of our ESR-energy to BIC and GAP, and also include two $L = 1$ baselines that use eigenvalue magnitude and exact-mode norm as the per-mode scores along with the binary mode selection framework (Algorithm 2).

Even without delay-coordinates, ESR-energy remains interpretable and reliable across all tested ranges of SNR, $\Delta\theta$, and damping parameter ρ . In this setting, eigenvalue magnitude and mode-norm baselines behave similarly but become reliable sooner, with eigenvalue magnitude consistently outperforming mode norm. This supports the analysis in Sec. VIB, and also shows that ESR-energy retains practical value when delay-coordinates are infeasible or undesirable.

Table II reports the corresponding normalized AUC values for the no-delay setting.

C. Spurious eigenvalue behavior under delay-coordinates

To test the effect of the embedding length L on spurious eigenvalues, we fix $m = 3$ and $M = 15$ and run 500 trials. For each L , we pool the magnitudes $|\hat{\lambda}_j|$ of all spurious eigenvalues across all trials and compute the empirical CDF.

Figure 3 shows that the distribution of spurious eigenvalue magnitudes shifts upward with L , increasingly concentrating near the unit circle. At the same time, the pooled distributions retain a non-negligible lower tail for all tested L , indicating substantial variability even when typical magnitudes are large.

This is the empirical observation highlighted in Sec. VIB: as L increases, the bulk of spurious eigenvalue magnitudes shifts toward the unit circle, while a substantial lower tail persists. Consequently, even at large L , eigenvalue magnitude alone cannot reliably separate true and spurious components.

VIII. CONCLUSIONS

Our results indicate that, in delay-coordinates DMD, model order detection is fundamentally governed by subspace geometry rather than by spectral magnitude. The most informative signals for mode selection are encoded in the induced spatiotemporal organization of the modes. Consistent with

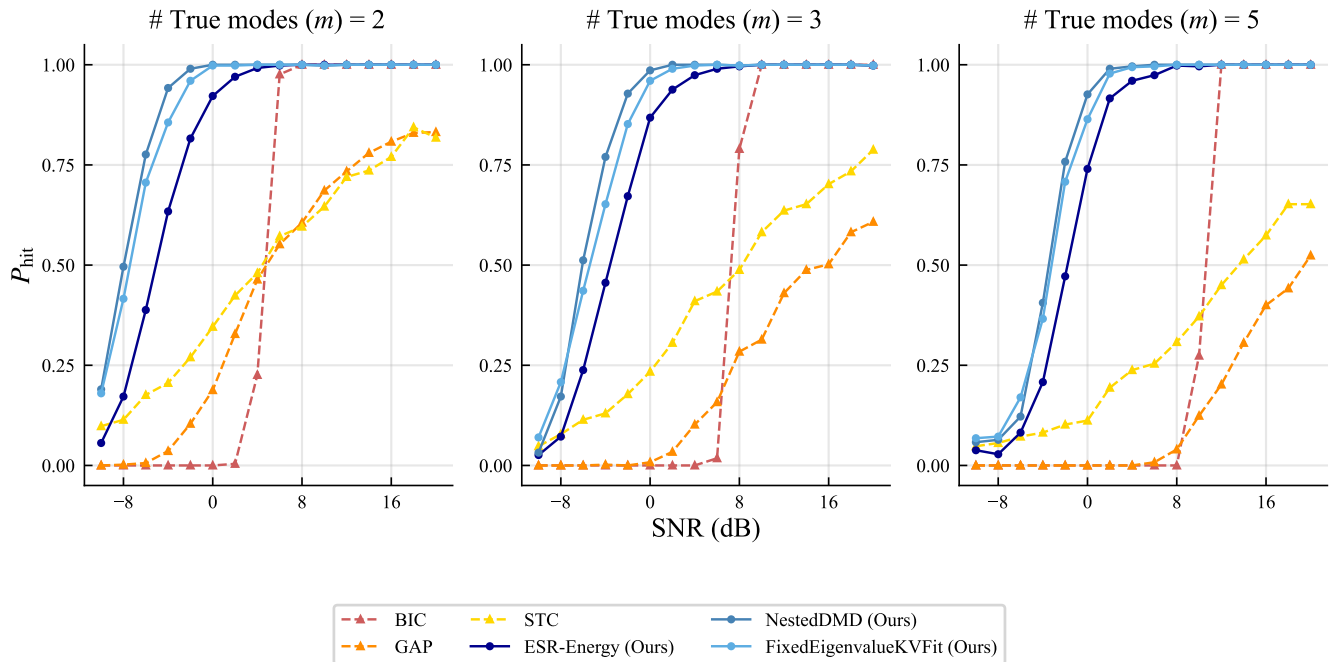


FIG. 4. Order-hit probability vs. SNR under Gaussian noise. Panels show $m = 2$ (left), $m = 3$ (center), and $m = 5$ (right). Working point: $N = 200$, $D = 45$, $L = 64$, $M = 15$; eigenvalues satisfy $\rho_j = 0.98$ with equally spaced phases and minimal separation $\Delta\theta = 0.01$; all amplitudes equal to one. Only the SNR varies.

Method	$m = 2$					$m = 3$					$m = 5$				
	SNR	$\Delta\theta$	r	κ_b	M	SNR	$\Delta\theta$	r	κ_b	M	SNR	$\Delta\theta$	r	κ_b	M
BIC	0.497	0.811	0.154	0.507	0.994	0.400	0.690	0.149	0.290	0.992	0.320	0.594	0.122	0.025	0.265
GAP	0.424	0.629	0.137	0.064	0.680	0.212	0.590	0.120	0.034	0.317	0.122	0.574	0.111	0.013	0.107
STC	0.477	0.610	0.287	0.559	0.251	0.392	0.494	0.208	0.461	0.212	0.282	0.356	0.145	0.332	0.153
ESR-Energy	0.813	0.955	0.413	0.973	0.646	0.764	0.876	0.303	0.971	0.639	0.707	0.807	0.264	0.930	0.605
NestedDMD	0.913	0.962	0.575	0.994	0.949	0.849	0.894	0.397	0.992	0.931	0.774	0.826	0.320	0.985	0.868
FixedEigenvalueKVFit	0.895	0.962	0.567	0.992	0.966	0.833	0.894	0.410	0.990	0.947	0.767	0.828	0.336	0.984	0.884

TABLE I. Normalized AUC for DC experiments (delay-embedded) across one-dimensional parameter sweeps. Columns grouped by number of true modes (m) contain AUC values for: SNR, phase separation ($\Delta\theta$), damping coefficient (r), amplitude ratio ($\kappa_b = b_{\max}/b_{\min}$), and order-overestimation (M). Boldface denotes the best score in each column.

this outcome, the KV-deviation criteria, which explicitly test delay-induced structure, are the most reliable across the tested regimes and outperform both classical baselines and the ESR-based method. Moreover, the spurious spectrum is not invariant under delay-coordinates: spurious eigenvalue magnitudes grow systematically with the embedding length L . This behavior helps explain why the mode-norm method, which is often effective in standard ($L = 1$) DMD, can lose discriminative power in delay-coordinates. These findings support the central claim of this work: true and spurious modes are best distinguished not by global spectral summaries, but by their geometric alignment with signal-dominated subspaces and their conformity to delay-induced structural organization.

An additional conceptual message of our analysis concerns the relationship between DMD and the unconstrained least-squares (LS) problem used to approximate temporal evolution. By exploiting the tight connection between truncation in DMD and rank-constrained LS formulations, we show that

truncation manifests geometrically as a deviation of the computed modes from the ideal KV structure induced by delay-coordinates. Moreover, by linking this structural deviation to signal-subspace geometry through the ESR, we demonstrate that it is not uniform across modes: signal-consistent (true) modes adhere more strongly to the KV structure, while spurious modes exhibit systematically larger departures. This perspective clarifies how finite-rank approximation reshapes the mode geometry and provides a unified interpretation of residual- and structure-based selection criteria. In addition, it reveals that truncation in DMD is not merely a numerical device, but a structural operation that reshapes the companion-induced organization of the modes in a mode-dependent manner.

A practical consideration is sensitivity to the hyper-parameters L and M . The embedding length L should be selected for modeling and spectral estimation, not for detection. Empirically, our methods are effective from modest L

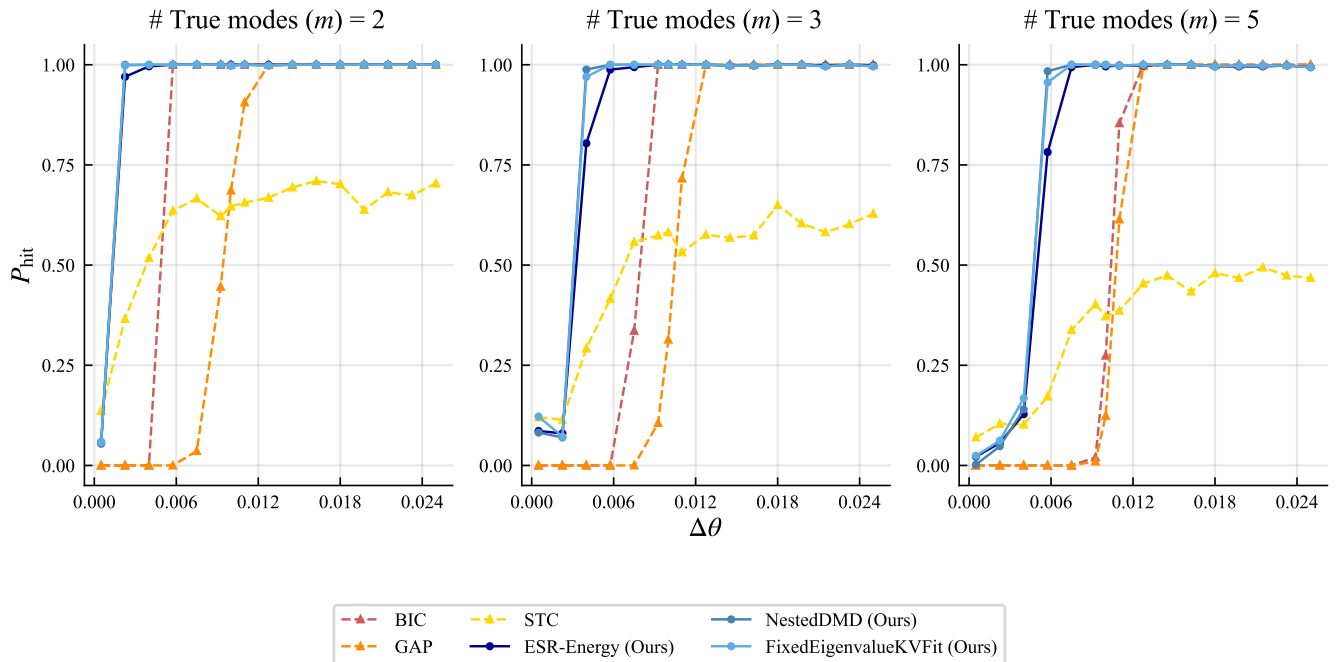


FIG. 5. Order-hit probability vs. phase separation $\Delta\theta$ (defined in (44)) under Gaussian noise. Panels show $m = 2$ (left), $m = 3$ (center), and $m = 5$ (right). Working point matches Fig. 4, with SNR fixed at 10 dB; only $\Delta\theta$ varies.

Method	$m = 2$				$m = 3$				$m = 5$			
	SNR	$\Delta\theta$	r	κ_b	SNR	$\Delta\theta$	r	κ_b	SNR	$\Delta\theta$	r	κ_b
BIC	0.759	0.961	0.910	0.995	0.619	0.856	0.356	0.987	0.476	0.735	0.214	0.819
GAP	0.453	0.627	0.132	0.069	0.222	0.592	0.119	0.033	0.135	0.575	0.113	0.015
ESR-Energy	0.988	0.963	0.996	0.998	0.899	0.886	0.498	0.991	0.793	0.812	0.291	0.987
ExactModeNorm	1.000	0.996	1.000	1.000	0.984	0.961	0.677	0.996	0.867	0.885	0.363	0.990
EigenvalueMagnitude	1.000	1.000	1.000	1.000	0.992	0.961	0.726	0.996	0.894	0.885	0.378	0.990

TABLE II. Normalized AUC for No-DC experiments ($L = 1$, no delays) across one-dimensional parameter sweeps. Columns grouped by number of true modes (m) contain AUC values for: SNR, phase separation ($\Delta\theta$), damping coefficient (r), and amplitude ratio ($\kappa_b = b_{\max}/b_{\min}$). Boldface denotes the best score in each column.

values and do not deteriorate as L grows. The truncation rank M is best interpreted through the overestimation gap $M - m$: while M must exceed m to allow post hoc mode selection, overly large M shrinks residual energy for all modes and can reduce the discriminative power of the ESR. This sensitivity suggests that richer geometric descriptors, such as the distribution of mode energy across singular directions, may provide more stable information than an aggregated residual summary alone. In contrast, the KV-deviation criteria largely mitigate the dependence on M , remaining reliable even under aggressive overestimation.

Several future directions appear promising. First, it would be valuable to characterize how true and spurious modes distribute energy across singular directions and to develop selection rules that exploit distributional differences directly. Second, we observe that spurious spectral statistics vary systematically with the embedding length L ; explaining the mechanism behind this dependence would deepen our understanding of how delay-coordinates reshape the spurious spectrum. Finally, although the ESR and KV deviations are conceptually

linked through the companion eigenrelation, developing a unified theory that quantitatively links residual geometry, KV conformity, and spectral statistics under delay embedding remains an important open direction.

AUTHOR DECLARATIONS

Conflict of Interest

The authors have no conflicts to disclose.

Author Contributions

Yoav Harris: Conceptualization (equal); Formal analysis (lead); Investigation (lead); Methodology (lead); Software (lead); Validation (lead); Visualization (lead); Writing – original draft (lead); Writing – review & editing (equal).

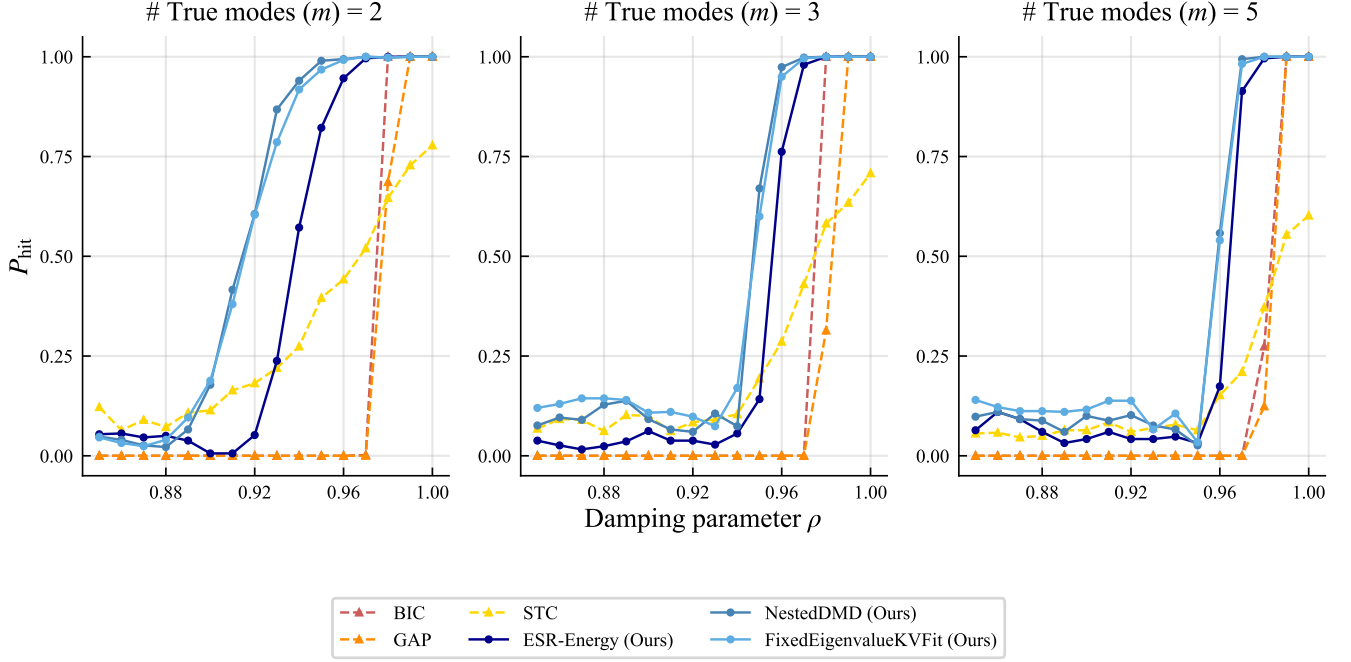


FIG. 6. Order-hit probability vs. damping factor ρ under Gaussian noise. Panels show $m = 2$ (left), $m = 3$ (center), and $m = 5$ (right). Working point matches Figs. 4–5; only ρ varies.

Hadas Benisty: Conceptualization (equal); Funding acquisition (equal); Supervision (equal); Writing – review & editing (equal). **Ronen Talmon:** Conceptualization (equal); Funding acquisition (equal); Supervision (equal); Writing – review & editing (equal).

DATA AVAILABILITY STATEMENT

The data that support the findings of this study are available within the article. The data were generated via numerical simulations, and the Python code used to generate the data and reproduce the figures is available on GitHub at <https://github.com/YoavHarris/geometric-dc-dmd-order-detection>. A citable archival release is available via Zenodo⁴⁷.

APPENDICES

Appendix A: Relations between D , L and N

This appendix revisits several identities from the main text in the *wide* delay-embedded setting, where the snapshot matrix $\mathbf{X}_0 \in \mathbb{C}^{DL \times (N-L)}$ satisfies

$$DL < N - L. \quad (\text{A1})$$

In this regime, \mathbf{X}_0 has more columns than rows. Throughout we assume that \mathbf{X}_0 has full row rank,

$$\text{rank}(\mathbf{X}_0) = DL, \quad (\text{A2})$$

which is a generic outcome under sufficiently rich excitation or additive noise.

Full row rank implies that $\mathbf{X}_0 \mathbf{X}_0^H$ is invertible and that the Moore–Penrose pseudoinverse admits the form

$$\mathbf{X}_0^\dagger = \mathbf{X}_0^H (\mathbf{X}_0 \mathbf{X}_0^H)^{-1}. \quad (\text{A3})$$

Let $\mathcal{U} = \text{col}(\mathbf{X}_0)$ and denote by $\mathbf{P}_{\mathcal{U}}$ the orthogonal projector onto \mathcal{U} . Since $\text{rank}(\mathbf{X}_0) = DL$, we have $\mathcal{U} = \mathbb{C}^{DL}$ and therefore

$$\mathbf{P}_{\mathcal{U}} = \mathbf{I}_{DL}. \quad (\text{A4})$$

Consequently, the least-squares propagator

$$\mathbf{A}_{\text{MP}} = \mathbf{X}_1 \mathbf{X}_0^\dagger \quad (\text{A5})$$

is uniquely defined.

This identity has immediate implications for residual-based diagnostics. Because $\mathcal{U} = \mathbb{C}^{DL}$, there is no component outside \mathcal{U} ; in particular, for an exact DMD mode $\hat{\phi}^e$ the decomposition

$$\hat{\phi}^e = \mathbf{P}_{\mathcal{U}_M} \hat{\phi}^e + (\mathbf{P}_{\mathcal{U}} - \mathbf{P}_{\mathcal{U}_M}) \hat{\phi}^e + (\mathbf{I} - \mathbf{P}_{\mathcal{U}}) \hat{\phi}^e \quad (\text{A6})$$

reduces to

$$\hat{\phi}^e = \mathbf{P}_{\mathcal{U}_M} \hat{\phi}^e + (\mathbf{I} - \mathbf{P}_{\mathcal{U}_M}) \hat{\phi}^e, \quad (\text{A7})$$

because $(\mathbf{I} - \mathbf{P}_{\mathcal{U}}) \hat{\phi}^e = \mathbf{0}$. Thus, residual-type scores relative to \mathcal{U}_M quantify only the truncation effect $(\mathbf{I} - \mathbf{P}_{\mathcal{U}_M}) \hat{\phi}^e$, which shrinks monotonically as M increases toward $\min(DL, N -$

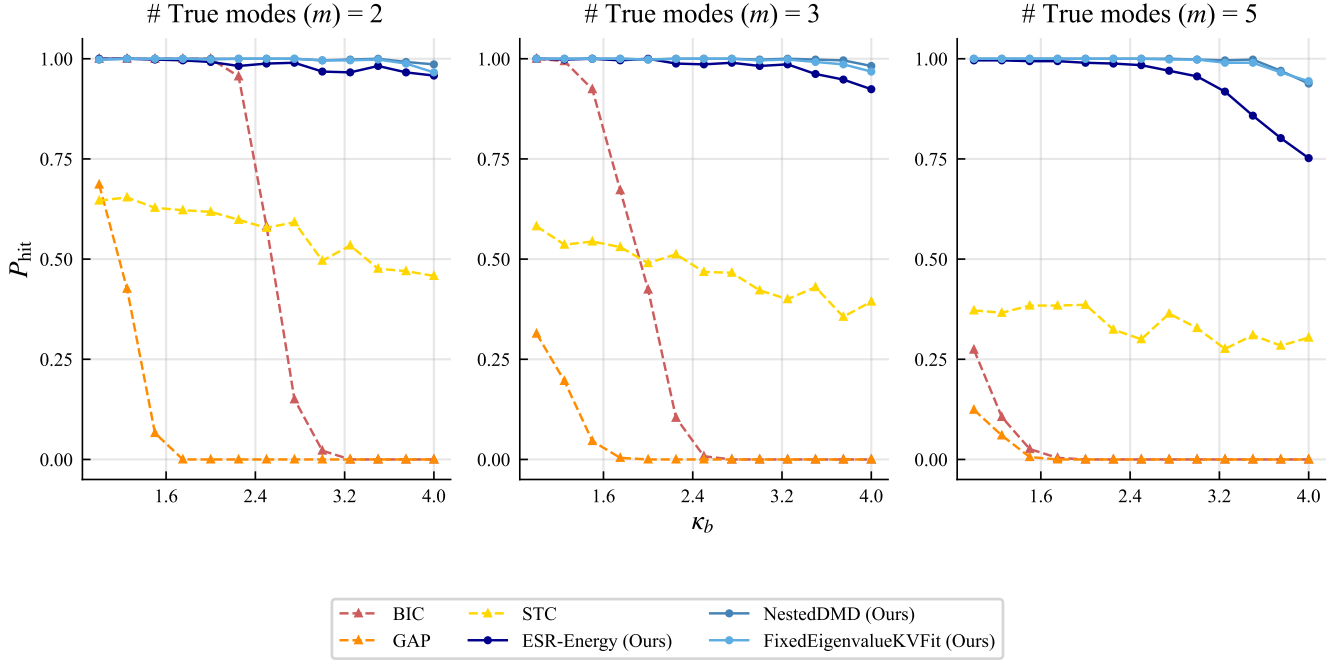


FIG. 7. Order-hit probability vs. amplitude heterogeneity κ_b (defined in (45)) under Gaussian noise. Panels show $m = 2$ (left), $m = 3$ (center), and $m = 5$ (right). As κ_b increases, the baseline methods (STC, BIC, GAP) degrade, while the KV-deviation methods and ESR-energy remain accurate across most of the tested range. Working point matches Figs. 4–6.

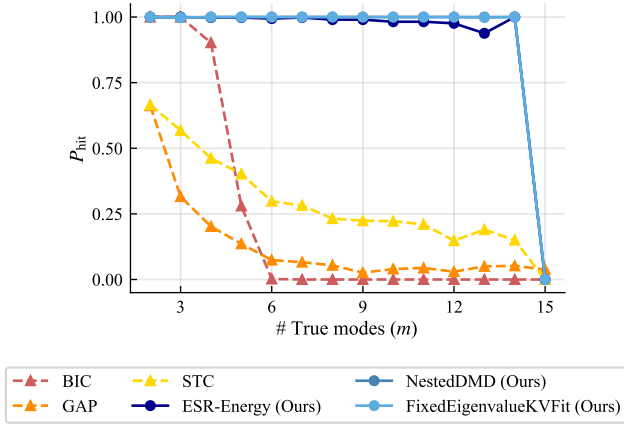


FIG. 8. Order-hit probability vs. number of true modes m under Gaussian noise. Working point matches Fig. 4. Our methods remain effective for complex signals where baselines deteriorate rapidly.

$L) = DL$. In other words, the wide full-row-rank regime is an extreme case in which $P_{\mathcal{U}} = I_{DL}$ and residual-type scores relative to \mathcal{U}_M reflect only the truncation term $(\mathbf{I} - P_{\mathcal{U}_M})\hat{\phi}^e$, which shrinks to zero as $M \uparrow DL$. We therefore focus on the more common tall regime $N - L < DL$, which is typical in high-dimensional measurements (and even more so under delay coordinates) and is also more challenging from an estimation standpoint since fewer delay vectors are available relative to the number of unknown parameters.

The same simplification carries over to the block-companion structure. In the delay-embedded construction, the shift relations in the first $L - 1$ block rows hold exactly by definition, so the block-companion matrix C_L is feasible for the constrained least-squares problem that enforces these shift equations. In the wide full-row-rank regime, the identity $A_{\text{MP}} = C_L P_{\mathcal{U}}$ simplifies (since $P_{\mathcal{U}} = I_{DL}$) to

$$A_{\text{MP}} = C_L. \tag{A8}$$

Hence the Moore–Penrose solution already acts as an exact shift on all DL coordinates, and no additional projection through $P_{\mathcal{U}}$ takes place.

Appendix B: Choosing the signal-aligned subspace

The best m -dimensional proxy to \mathcal{S} within \mathcal{U}_M is not necessarily given by the span of the leading m singular vectors. More generally, \mathcal{U}_m may be defined as the span of the m singular vectors (among the leading M) that minimize the projector distance (cf. (22)) to \mathcal{S} :

$$\mathcal{U}_m := \text{col}(U_{\mathcal{I}_m}), \tag{B1}$$

where $U_{\mathcal{I}}$ denotes the matrix consisting of the singular vectors $\{u_i\}_{i \in \mathcal{I}}$ for an index set $\mathcal{I} \subset \{1, \dots, M\}$. The optimal index set is defined by

$$\mathcal{I}_m \in \arg \min_{\mathcal{I} \subset \{1, \dots, M\}, |\mathcal{I}|=m} \|P_{\mathcal{S}} - P_{\text{col}(U_{\mathcal{I}})}\|_2, \tag{B2}$$

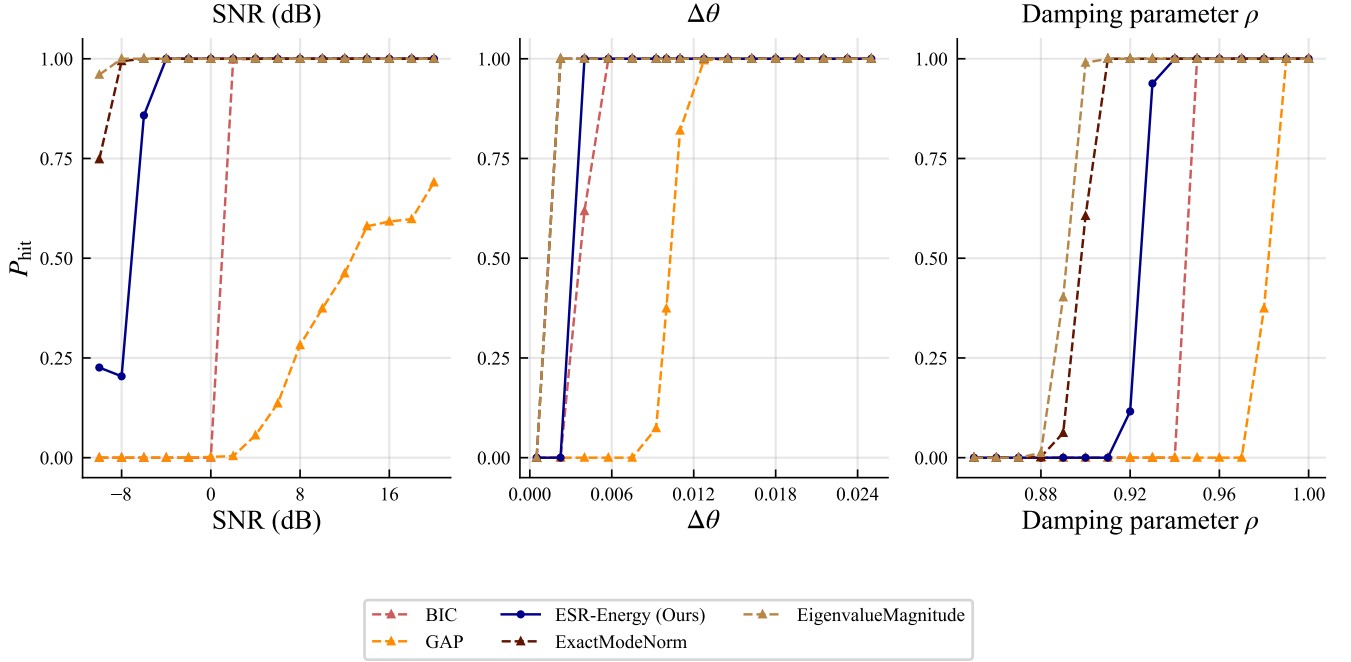


FIG. 9. Order detection performance without delay-coordinates ($L = 1$). Representative parameter variations under Gaussian noise for $m = 3$ over SNR (left), phase separation $\Delta\theta$ (middle), and damping ρ (right). For SNR, ESR-energy becomes reliable at lower levels than BIC, while mode-norm and eigenvalue-magnitude detectors become reliable sooner still, with eigenvalue magnitude performing best. For $\Delta\theta$, the methods remain close, with ESR-energy only slightly earlier at the transition, and again mode norm and eigenvalue magnitude shifting the transition earlier (eigenvalue magnitude best). GAP is unreliable across the tested ranges. Working point matches Figs. 4–7, except that $L = 1$ and $D = 220$.

where $\mathbf{P}_{\text{col}(\mathbf{U}_{\mathcal{I}})}$ denotes the orthogonal projector onto $\text{col}(\mathbf{U}_{\mathcal{I}})$.

This construction is conceptual, since \mathcal{S} , and hence the optimal index set \mathcal{I}_m , are unknown in practice. It serves to formalize the ideal signal-consistent subspace against which computed modes are compared.

Appendix C: Bound on signal–subspace deviation under noise

This appendix specializes classical subspace perturbation theory to the delay-embedded trajectory matrix and quantifies the deviation between the true signal subspace

$$\mathcal{S} = \text{col}(\mathbf{S}_0)$$

and its empirical estimate $\text{col}(\mathbf{U}_m)$, where \mathbf{U}_m contains the leading m left singular vectors of

$$\mathbf{X}_0 = \mathbf{S}_0 + \mathbf{E}.$$

Model and notation

The clean signal follows the exponential model

$$\mathbf{s}_k = \sum_{j=1}^m b_j \phi_j \lambda_j^k, \quad \lambda_j = \rho_j e^{i\theta_j},$$

with spatial vectors $\phi_j \in \mathbb{C}^D$. We assume a bounded-radius regime $0 < \rho_{\min} \leq \rho_j \leq \rho_{\max} \leq 1$.

Let N denote the number of samples $\{\mathbf{s}_k\}_{k=0}^{N-1}$. After delay embedding with L delays, the number of usable delay vectors is

$$N_{\text{eff}} := N - L + 1,$$

and the standard DC–DMD snapshot matrices satisfy

$$\mathbf{X}_0, \mathbf{X}_1 \in \mathbb{C}^{DL \times (N-L)}.$$

In particular, the noiseless part of \mathbf{X}_0 admits the factorization

$$\mathbf{S}_0 = \tilde{\Phi}_L \mathbf{B} \mathbf{V}_{N-L}^\top,$$

where the lifted spatial factor is

$$\tilde{\Phi}_L := \mathbf{V}_L \odot \Phi = [\mathbf{v}_L(\lambda_1) \otimes \phi_1 \cdots \mathbf{v}_L(\lambda_m) \otimes \phi_m] \in \mathbb{C}^{DL \times m},$$

with base spatial factor $\Phi = [\phi_1 \cdots \phi_m]$. The amplitudes are given by $\mathbf{B} = \text{diag}(b_1, \dots, b_m)$, and the Vandermonde matrix is defined generally as

$$\mathbf{V}_n = [\mathbf{v}_n(\lambda_1) \cdots \mathbf{v}_n(\lambda_m)] \in \mathbb{C}^{n \times m},$$

$$\mathbf{v}_n(\lambda) = [1, \lambda, \dots, \lambda^{n-1}]^\top.$$

Let θ_{\max} denote the largest principal angle between $\text{col}(\mathbf{U}_m)$ and \mathcal{S} .

Assumptions

We assume:

(A1) *Phase separation*:

$$\Delta_\theta := \min_{j \neq j'} \min(|\theta_j - \theta_{j'}|, 2\pi - |\theta_j - \theta_{j'}|) > 0.$$

(A2) *Nondegeneracy*: $\sigma_m(\Phi) > 0$ and $\min_j |b_j| > 0$.

(A3) L and $N - L$ exceed a constant multiple of $1/\Delta_\theta$.

Signal–subspace deviation

Lemma 3.1 (Signal–subspace deviation). *If $\|\mathbf{E}\|_2$ is sufficiently small, then*

$$\|\mathbf{P}_{\text{col}(\mathbf{U}_m)} - \mathbf{P}_S\|_2 = \sin \theta_{\max} \leq \eta,$$

where

$$\eta = \frac{\|\mathbf{E}\|_2}{\sigma_m(\Phi) \min_j |b_j| \alpha_L \alpha_{N-L} - \|\mathbf{E}\|_2}.$$

Here α_n denotes any lower bound on $\sigma_m(\mathbf{V}_n)$ valid under assumptions (A1)–(A3).

Sketch. Wedin’s $\sin \Theta$ theorem gives

$$\sin \theta_{\max} \leq \frac{\|\mathbf{E}\|_2}{\sigma_m(\mathbf{S}_0) - \|\mathbf{E}\|_2}.$$

Using the factorization of \mathbf{S}_0 ,

$$\sigma_m(\mathbf{S}_0) \geq \sigma_m(\tilde{\Phi}_L) \min_j |b_j| \sigma_m(\mathbf{V}_{N-L}).$$

Since $\tilde{\Phi}_L = \mathbf{V}_L \odot \Phi$,

$$\sigma_m(\tilde{\Phi}_L) \geq \sigma_m(\Phi) \sigma_m(\mathbf{V}_L).$$

Combining the inequalities and using $\sigma_m(\mathbf{V}_n) \geq \alpha_n$ yields the result. \square

Vandermonde conditioning

Under (A1), classical results on Vandermonde conditioning imply that

$$\sigma_m(\mathbf{V}_n) \geq \alpha_n,$$

for some $\alpha_n > 0$ depending on the minimal phase gap Δ_θ , the order m , and the bounded-radius regime $[\rho_{\min}, \rho_{\max}]$. Smaller phase gaps worsen the conditioning and reduce α_n . When $\rho_{\max} = 1$ (unit-modulus nodes), one may take a bound of the form

$$\alpha_n \geq c_{\text{sep}}(\Delta_\theta, m) \sqrt{n},$$

whereas for $\rho_{\max} < 1$ the dependence on n need not exhibit the same \sqrt{n} growth and may level off, with constants controlled additionally by $[\rho_{\min}, \rho_{\max}]$. See, e.g.,^{48,49}

Discussion

The deviation $\sin \theta_{\max}$ scales linearly with $\|\mathbf{E}\|_2$ and is controlled by the conditioning of the lifted signal factors. The dependence on L and $N - L$ enters through the Vandermonde conditioning constants α_L and α_{N-L} ; when $\rho_{\max} = 1$ this recovers the familiar $\sqrt{L(N-L)}$ scaling, while for $\rho_{\max} < 1$ the improvement with n may saturate. The result provides a quantitative justification for Assumption 2.1 in the main text.

Appendix D: Delay-coordinates yield Kronecker–Vandermonde spatiotemporal modes

This appendix gives a short data-side derivation of the structural result identified in Ref. 29: a signal that is a sum of spatially modulated exponentials in time becomes, after delay-coordinates, a sum of spatiotemporally coupled KV templates, each still modulating a temporal exponential across the embedded columns. The argument requires no operator assumptions and applies only to the true components, providing a concise complement to the operator-side derivation in Sec. V, which extends the KV characterization to *all* modes (true and spurious).

Signal model

We adopt the exponential signal model from (6). For an embedding length L , collect L successive samples into

$$\tilde{\mathbf{s}}_k = \begin{bmatrix} \mathbf{s}_k \\ \mathbf{s}_{k+1} \\ \vdots \\ \mathbf{s}_{k+L-1} \end{bmatrix} \in \mathbb{C}^{DL}.$$

Embedding of a single exponential component

For the j th component $b_j \phi_j \lambda_j^k$,

$$\tilde{\mathbf{s}}_k^{(j)} = b_j \begin{bmatrix} \phi_j \lambda_j^k \\ \phi_j \lambda_j^{k+1} \\ \vdots \\ \phi_j \lambda_j^{k+L-1} \end{bmatrix} = b_j (\psi_L(\lambda_j) \otimes \phi_j) \lambda_j^k,$$

where $\psi_L(\lambda_j) = [1, \lambda_j, \dots, \lambda_j^{L-1}]^\top$. Delay-coordinates therefore fuse the spatial vector ϕ_j and temporal exponential λ_j^k into the KV template $\psi_L(\lambda_j) \otimes \phi_j$.

KV decomposition of the embedded trajectory matrix

Let $N_{\text{eff}} = -L + 1$ be the number of embedded columns. The trajectory matrix becomes

$$\tilde{\mathbf{S}} = \sum_{j=1}^m b_j (\psi_L(\lambda_j) \otimes \phi_j) [1, \lambda_j, \dots, \lambda_j^{N_{\text{eff}}-1}].$$

Writing $\psi_{N_{\text{eff}}}(\lambda_j)$ for the temporal Vandermonde vector, this is

$$\tilde{\mathbf{S}} = \sum_{j=1}^m b_j (\psi_L(\lambda_j) \otimes \phi_j) \psi_{N_{\text{eff}}}(\lambda_j)^\top.$$

Conclusion

Under delay-coordinates, every true component becomes a KV term whose spatial and temporal factors are inseparably coupled. These are the ideal KV templates assumed in Bronstein *et al.*²⁹. The operator-side analysis of Sec. V generalizes this perspective by showing that *all* projected-DMD modes, including spurious ones, satisfy an approximate KV relation whose deviation is measured by their estimated-subspace residual.

Appendix E: Block-Companion Structure and Least-Squares Propagators

We consider the least-squares problem

$$\min_{\mathbf{A} \in \mathbb{C}^{DL \times DL}} \|\mathbf{A}\mathbf{X}_0 - \mathbf{X}_1\|_F^2,$$

with delay-embedded snapshot matrices $\mathbf{X}_0, \mathbf{X}_1 \in \mathbb{C}^{DL \times N_{\text{eff}}}$. Among all minimizers we single out the Moore–Penrose (minimum-norm) minimizer

$$\mathbf{A}_{\text{MP}} := \mathbf{X}_1 \mathbf{X}_0^\dagger,$$

which will be related to the reduced propagator via an orthogonal projection.

1. Existence of a block-companion minimizer

Partition \mathbf{A} into $D \times D$ block rows

$$\mathbf{A} = \begin{bmatrix} \mathbf{A}^{(0)} \\ \vdots \\ \mathbf{A}^{(L-1)} \end{bmatrix}, \quad \mathbf{A}^{(\ell)} \in \mathbb{C}^{D \times DL}.$$

The objective splits as

$$\|\mathbf{A}\mathbf{X}_0 - \mathbf{X}_1\|_F^2 = \sum_{\ell=0}^{L-1} \|\mathbf{A}^{(\ell)} \mathbf{X}_0 - \mathbf{X}_1^{(\ell)}\|_F^2.$$

In DC–DMD,

$$\mathbf{X}_1^{(\ell)} = \mathbf{S}_L^{(\ell)} \mathbf{X}_0, \quad \ell = 0, \dots, L-2,$$

for the block-shift matrix \mathbf{S}_L . Thus setting $\mathbf{A}^{(\ell)} = \mathbf{S}_L^{(\ell)}$ for $\ell < L-1$ is already optimal. Minimizing only the last block row yields some \mathbf{B} , giving the block-companion minimizer

$$\mathbf{C}_L = \mathbf{S}_L + (e_L \otimes \mathbf{I}_D) \mathbf{B}.$$

Minimizing only the last block row amounts to

$$\min_{\mathbf{B} \in \mathbb{C}^{D \times DL}} \|\mathbf{B}\mathbf{X}_0 - \mathbf{X}_1^{(L-1)}\|_F^2.$$

Throughout, we fix

$$\mathbf{B} := \mathbf{X}_1^{(L-1)} \mathbf{X}_0^\dagger,$$

the Moore–Penrose least-squares predictor.

2. Eigenvectors of the block-companion matrix are KV

Let

$$\mathbf{C}_L = \begin{bmatrix} \mathbf{0} & \mathbf{I}_D & & \\ & \ddots & \ddots & \\ & & \mathbf{0} & \mathbf{I}_D \\ \mathbf{B}_1 & \mathbf{B}_2 & \cdots & \mathbf{B}_L \end{bmatrix}.$$

Write an eigenvector as

$$\mathbf{v} = [\mathbf{v}^{(0)}; \dots; \mathbf{v}^{(L-1)}].$$

For $\ell = 0, \dots, L-2$,

$$\mathbf{v}^{(\ell+1)} = \lambda \mathbf{v}^{(\ell)},$$

so $\mathbf{v}^{(\ell)} = \lambda^\ell \mathbf{v}^{(0)}$. The final block row imposes

$$(\mathbf{B}_1 + \lambda \mathbf{B}_2 + \cdots + \lambda^{L-1} \mathbf{B}_L) \mathbf{v}^{(0)} = \lambda^L \mathbf{v}^{(0)}.$$

Hence every eigenvector has KV form

$$\mathbf{v} = \mathbf{v}_L(\lambda) \otimes \mathbf{v}^{(0)}, \quad \mathbf{v}_L(\lambda) = [1, \lambda, \dots, \lambda^{L-1}]^\top.$$

3. The Moore–Penrose minimizer satisfies $\mathbf{X}_1 \mathbf{X}_0^\dagger = \mathbf{C}_L \mathbf{P}_U$

Let $\mathcal{U} = \text{col}(\mathbf{X}_0)$ and \mathbf{P}_U its projector.

Lemma 5.1 (Moore–Penrose projection identity). *Let $\mathcal{U} = \text{col}(\mathbf{X}_0)$ and let*

$$\mathbf{P}_U := \mathbf{X}_0 \mathbf{X}_0^\dagger$$

be the orthogonal projector onto \mathcal{U} . Consider the least-squares problem

$$\min_{\mathbf{A} \in \mathbb{C}^{DL \times DL}} \|\mathbf{A}\mathbf{X}_0 - \mathbf{X}_1\|_F^2,$$

and define the Moore–Penrose (minimum-norm) minimizer

$$\mathbf{A}_{\text{MP}} := \mathbf{X}_1 \mathbf{X}_0^\dagger.$$

Then, for any minimizer \mathbf{A}_\star ,

$$\mathbf{A}_{\text{MP}} = \mathbf{A}_\star \mathbf{P}_U.$$

Proof. Any minimizer \mathbf{A}_\star satisfies the normal equations

$$(\mathbf{A}_\star \mathbf{X}_0 - \mathbf{X}_1) \mathbf{X}_0^H = \mathbf{0},$$

equivalently,

$$\mathbf{A}_\star \mathbf{X}_0 \mathbf{X}_0^H = \mathbf{X}_1 \mathbf{X}_0^H.$$

A standard characterization of the solution set of this Frobenius least-squares problem is

$$\mathbf{A}_\star = \mathbf{X}_1 \mathbf{X}_0^\dagger + \mathbf{Z}(\mathbf{I} - \mathbf{P}_U), \quad \mathbf{Z} \in \mathbb{C}^{DL \times DL}.$$

Right-multiplying by \mathbf{P}_U and using $\mathbf{P}_U(\mathbf{I} - \mathbf{P}_U) = \mathbf{0}$ yields

$$\mathbf{A}_\star \mathbf{P}_U = (\mathbf{X}_1 \mathbf{X}_0^\dagger + \mathbf{Z}(\mathbf{I} - \mathbf{P}_U)) \mathbf{P}_U = \mathbf{X}_1 \mathbf{X}_0^\dagger = \mathbf{A}_{\text{MP}}.$$

□

4. The reduced propagator is the orthogonal compression of \mathbf{C}_L

Let $\mathbf{X}_0 = \mathbf{U}\mathbf{\Sigma}\mathbf{V}^H$ be the SVD and let \mathbf{U}_M be its first M columns. Define the reduced propagator

$$\mathbf{A}_M := \mathbf{U}_M^H \mathbf{A}_{\text{MP}} \mathbf{U}_M.$$

Lemma 5.2. *With \mathbf{C}_L from Subsection E 1,*

$$\mathbf{A}_M = \mathbf{U}_M^H \mathbf{C}_L \mathbf{U}_M.$$

Proof. From Lemma 5.1, $\mathbf{A}_{\text{MP}} = \mathbf{C}_L \mathbf{P}_U$. Since $\mathcal{U}_M \subset \mathcal{U}$, we have $\mathbf{P}_U \mathbf{U}_M = \mathbf{U}_M$, hence

$$\mathbf{A}_M = \mathbf{U}_M^H \mathbf{A}_{\text{MP}} \mathbf{U}_M = \mathbf{U}_M^H \mathbf{C}_L \mathbf{U}_M.$$

□

5. Proof of Theorem 5.4

Proof. Fix an eigenpair $(\hat{\lambda}_j, \mathbf{w}_j)$ of \mathbf{A}_M from (13), and let $\hat{\phi}_j^p$ and $\hat{\phi}_j^e$ be the associated projected and exact DMD modes from (14) and (16). Recall that $\hat{\phi}_j^p \in \mathcal{U}_M$, so $\mathbf{P}_{\mathcal{U}_M} \hat{\phi}_j^p = \hat{\phi}_j^p$.

We begin by projecting the exact mode onto \mathcal{U}_M and identifying the reduced propagator within the expression. Using (16),

$$\mathbf{P}_{\mathcal{U}_M} \hat{\phi}_j^e = \mathbf{U}_M \underbrace{(\mathbf{U}_M^H \mathbf{X}_1 \mathbf{V}_M \mathbf{\Sigma}_M^{-1})}_{\mathbf{A}_M} \mathbf{w}_j = \mathbf{U}_M \mathbf{A}_M \mathbf{w}_j, \quad (\text{E1})$$

We now invoke the eigen-relation $\mathbf{A}_M \mathbf{w}_j = \hat{\lambda}_j \mathbf{w}_j$ and the definition of projected DMD modes (14) to obtain

$$\mathbf{P}_{\mathcal{U}_M} \hat{\phi}_j^e = \mathbf{U}_M \mathbf{A}_M \mathbf{w}_j = \hat{\lambda}_j \mathbf{U}_M \mathbf{w}_j = \hat{\lambda}_j \hat{\phi}_j^p. \quad (\text{E2})$$

Hence,

$$\mathbf{r}_{\mathcal{U}_M}(\hat{\phi}_j^e) = (\mathbf{I} - \mathbf{P}_{\mathcal{U}_M}) \hat{\phi}_j^e = \hat{\phi}_j^e - \hat{\lambda}_j \hat{\phi}_j^p. \quad (\text{E3})$$

Next, by Lemma 5.1 and the existence of the block-companion minimizer \mathbf{C}_L from Subsection E 1, we have

$$\mathbf{A}_{\text{MP}} = \mathbf{X}_1 \mathbf{X}_0^\dagger = \mathbf{C}_L \mathbf{P}_U, \quad \mathcal{U} = \text{col}(\mathbf{X}_0).$$

Since $\hat{\phi}_j^p = \mathbf{U}_M \mathbf{w}_j \in \mathcal{U}$, it follows that $\mathbf{P}_U \hat{\phi}_j^p = \hat{\phi}_j^p$ and thus

$$\mathbf{C}_L \hat{\phi}_j^p = \mathbf{A}_{\text{MP}} \hat{\phi}_j^p = \mathbf{X}_1 \mathbf{X}_0^\dagger \mathbf{U}_M \mathbf{w}_j.$$

Using the (untruncated) SVD $\mathbf{X}_0 = \mathbf{U}\mathbf{\Sigma}\mathbf{V}^H$ and the fact that \mathbf{U}_M consists of the first M columns of \mathbf{U} , we obtain

$$\mathbf{X}_0^\dagger \mathbf{U}_M = \mathbf{V}\mathbf{\Sigma}^{-1} \mathbf{U}^H \mathbf{U}_M = \mathbf{V}_M \mathbf{\Sigma}_M^{-1},$$

and therefore

$$\mathbf{C}_L \hat{\phi}_j^p = \mathbf{X}_1 \mathbf{V}_M \mathbf{\Sigma}_M^{-1} \mathbf{w}_j = \hat{\phi}_j^e$$

by (16). Combining with (E3) yields

$$(\mathbf{C}_L - \hat{\lambda}_j \mathbf{I}) \hat{\phi}_j^p = \hat{\phi}_j^e - \hat{\lambda}_j \hat{\phi}_j^p = \mathbf{r}_{\mathcal{U}_M}(\hat{\phi}_j^e),$$

which is (37). □

Appendix F: Fixed-Eigenvalue KV Fit (FEKVF)

The fixed-eigenvalue KV fit (FEKVF) provides a lightweight alternative to the nested rank-1 DMD of Sec. V B. After reshaping each projected mode into a per-mode lag matrix

$$\hat{\phi}_j^p \mapsto \hat{\mathbf{\Phi}}_j := \text{reshape}(\hat{\phi}_j^p, D \times L) \in \mathbb{C}^{D \times L},$$

FEKVF evaluates how well $\hat{\mathbf{\Phi}}_j$ conforms to a KV evolution that is consistent with its existing eigenvalue $\hat{\lambda}_j$. Unlike the nested fit, no inner DMD is performed; the eigenvalue is held fixed.

Closed-form residual

For the eigenvalue $\hat{\lambda}_j$, define the Vandermonde vector

$$\mathbf{a}_j := \mathbf{v}_L(\hat{\lambda}_j) = [1, \hat{\lambda}_j, \dots, \hat{\lambda}_j^{L-1}]^\top.$$

Projecting $\hat{\mathbf{\Phi}}_j$ onto the fixed-eigenvalue KV cone amounts to the rank-1 least-squares problem

$$\min_{\mathbf{u} \in \mathbb{C}^D} \|\hat{\mathbf{\Phi}}_j - \mathbf{u} \mathbf{a}_j^\top\|_F^2,$$

whose minimizer is

$$\mathbf{u}_j^\star = \frac{\hat{\mathbf{\Phi}}_j \mathbf{a}_j^\star}{\|\mathbf{a}_j\|_2^2}, \quad \hat{\mathbf{\Phi}}_j^{(\text{KV})} := \mathbf{u}_j^\star \mathbf{a}_j^\top.$$

The corresponding normalized residual is

$$\mathcal{R}_j^{(KV)} := \frac{\|\widehat{\Phi}_j - \widehat{\Phi}_j^{(KV)}\|_F^2}{DL}$$

We form a scalar KV-conformity score

$$\zeta_j := \log(\mathcal{R}_j^{(KV)} + \varepsilon),$$

where $\varepsilon > 0$ prevents singularities. Smaller values indicate closer agreement with the KV pattern implied by $\widehat{\lambda}_j$.

Computation

All operations in FEKVF reduce to one $D \times L$ matrix-vector product and a small number of scalar reductions per mode. In particular, no inner DMD problem is solved and the eigenvalue is reused rather than re-estimated. As a result, the per-mode effort is substantially smaller than for the nested rank-1 fit, and the procedure applies independently to each mode and is easily implemented in a batched fashion. A formal comparison of the asymptotic costs of FEKVF and nested DMD is given in Appendix G.

Require: Mode matrices $\{\widehat{\Phi}_j \in \mathbb{C}^{D \times L}\}_{j=1}^M$, eigenvalues $\{\widehat{\lambda}_j\}$, small $\varepsilon > 0$; clustering routine and aggregation rule as in Algorithm 2

Ensure: Order estimate \widehat{m} and labels $\{\ell_j\}$

- 1: **for** $j = 1, \dots, M$ **do**
- 2: $\mathbf{a} \leftarrow [1, \widehat{\lambda}_j, \dots, \widehat{\lambda}_j^{L-1}]^\top$
- 3: $\mathbf{w} \leftarrow \mathbf{a}^*$
- 4: $\mathbf{u}^* \leftarrow \widehat{\Phi}_j \mathbf{w} / \|\mathbf{a}\|_2^2$
- 5: $\widehat{\Phi}_j^{(KV)} \leftarrow \mathbf{u}^* \mathbf{a}^\top$
- 6: $\mathcal{R}_j^{(KV)} \leftarrow \|\widehat{\Phi}_j - \widehat{\Phi}_j^{(KV)}\|_F^2 / (DL)$
- 7: $\zeta_j \leftarrow \log(\mathcal{R}_j^{(KV)} + \varepsilon)$
- 8: **end for**
- 9: Stack $\zeta = [\zeta_1, \dots, \zeta_M]$
- 10: Apply binary mode selection framework (Algorithm 2) to obtain $\{\ell_j\}$ and \widehat{m}

Algorithm 4. Fixed-Eigenvalue KV Fit (FEKVF)

Remarks. FEKVF shares the same conceptual interpretation as the nested rank-1 DMD: both measure global KV conformity of the reconstructed mode trajectories. The key difference is that FEKVF holds the eigenvalue fixed and performs a single rank-1 projection, producing a scalar KV-conformity score ζ_j that feeds directly into the binary mode selection framework (Algorithm 2).

Appendix G: Computational Complexity of the Procedures

This appendix summarizes the computational costs associated with the procedures used throughout the paper. Throughout, D denotes the spatial dimension, L the embedding length, DL the lifted dimension, and $M > m$ the truncation rank.

1. DMD construction

The delay-embedded snapshot matrices $\mathbf{X}_0, \mathbf{X}_1 \in \mathbb{C}^{DL \times N}$ are processed by a rank- M SVD,

$$\mathbf{X}_0 \approx \mathbf{U}_M \mathbf{\Sigma}_M \mathbf{V}_M^\top.$$

Computing this truncated SVD has cost

$$O(DLN M),$$

which is the dominant cost in the full pipeline when N is not extremely small. The projected modes $\widehat{\phi}_j^p$ require a single matrix-vector multiplication per mode and cost $O(DLM)$ in total. Exact modes $\widehat{\phi}_j^e = \mathbf{X}_1 \mathbf{V}_M \mathbf{\Sigma}_M^{-1} \mathbf{e}_j$ require an additional multiplication by \mathbf{X}_1 , giving the same overall $O(DLM)$ cost.

2. Nested DMD and block-companion construction

The nested-DMD procedure (Section V B) applies a rank-1 DMD to each $D \times L$ mode matrix $\widehat{\Phi}_j$. The dominant operation per mode is a rank-1 SVD of a $D \times L$ matrix, which costs $O(DL)$. Running this for all M modes, and computing each residual $\mathcal{R}_j^{(KV)}$ (rank-1 outer product and Frobenius-norm difference, also $O(DL)$ per mode), gives total cost

$$O(DLM).$$

3. Fixed-eigenvalue KV fit (FEKVF)

FEKVF (Appendix F) also costs $O(DLM)$ in total, but with a smaller constant per mode: it replaces the rank-1 SVD with a single matrix-vector product $\widehat{\Phi}_j \mathbf{a}_j^* \in \mathbb{C}^D$ ($O(DL)$), followed by scalar reductions to evaluate $\mathcal{R}_j^{(KV)}$. FEKVF is therefore cheaper than nested DMD by the constant factor associated with eliminating the inner SVD per mode.

4. ESR-score computation

Each exact mode is a vector in \mathbb{C}^{DL} . Using the orthogonal decomposition (Sec. IV)

$$\widehat{\phi}_j^e = \widehat{\lambda}_j \widehat{\phi}_j^p + \mathbf{r}_{u_M}(\widehat{\phi}_j^e), \quad \|\widehat{\phi}_j^p\|_2 = 1,$$

the ESR score (residual energy) satisfies

$$\mathcal{R}_j = \|\mathbf{r}_{u_M}(\widehat{\phi}_j^e)\|_2^2 = \|\widehat{\phi}_j^e\|_2^2 - |\widehat{\lambda}_j|^2.$$

Thus no explicit projector applications are required, and evaluating all \mathcal{R}_j (and derived scalar scores such as ζ_j) over M modes costs

$$O(DLM),$$

with $O(M)$ additional memory.

5. Binary mode selection

The binary mode selection rule of Algorithm 2 operates on a per-mode scalar score $f_j \in \mathbb{R}$.

Clustering the M scalar scores into $k = 2$ groups (e.g., K-Means or a two-component GMM) costs

$$O(M)$$

per iteration for K-Means, and similarly

$$O(M)$$

per EM iteration for a diagonal-covariance GMM. In all cases, with $k = 2$, this clustering cost is negligible compared with the other steps of the pipeline.

REFERENCES

- ¹P. J. Schmid, *Journal of Fluid Mechanics* **656**, 5 (2010).
- ²G. Berkooz, P. Holmes, and J. L. Lumley, *Annual Review of Fluid Mechanics* **25**, 539 (1993).
- ³J. P. Cunningham and B. M. Yu, *Nature Neuroscience* **17**, 1500 (2014).
- ⁴M. M. Churchland, J. P. Cunningham, M. T. Kaufman, J. D. Foster, P. Nuyujukian, S. I. Ryu, and K. V. Shenoy, *Nature* **487**, 51 (2012).
- ⁵A. Hannachi, I. T. Jolliffe, and D. B. Stephenson, *International Journal of Climatology* **27**, 1119 (2007).
- ⁶D. W. J. Thompson and J. M. Wallace, *Journal of Climate* **13**, 1000 (2000).
- ⁷G. Kerschen, J. C. Golinval, A. F. Vakakis, and L. A. Bergman, *Nonlinear Dynamics* **41**, 147 (2005).
- ⁸A. Saito and T. Kuno, *Journal of Sound and Vibration* **481**, 115434 (2020).
- ⁹P. Benner, S. Gugercin, and K. Willcox, *SIAM Review* **57**, 483 (2015).
- ¹⁰J. H. Tu, C. W. Rowley, D. M. Luchtenburg, S. L. Brunton, and J. N. Kutz, *Journal of Computational Dynamics* **1**, 391 (2014).
- ¹¹J. N. Kutz, S. L. Brunton, B. W. Brunton, and J. L. Proctor, *Dynamic Mode Decomposition: Data-Driven Modeling of Complex Systems* (SIAM, 2016).
- ¹²C. W. Rowley, I. Mezić, S. Bagheri, P. Schlatter, and D. S. Henningson, *Journal of Fluid Mechanics* **641**, 115 (2009).
- ¹³M. Budišić, R. Mohr, and I. Mezić, *Chaos* **22**, 047510 (2012).
- ¹⁴M. J. Colbrook, *SIAM Review* **66**, 483 (2024).
- ¹⁵I. Mezić, *Nonlinear Dynamics* **41**, 309 (2005).
- ¹⁶I. Mezić, *Annual Review of Fluid Mechanics* **45**, 357 (2013).
- ¹⁷M. O. Williams, I. G. Kevrekidis, and C. W. Rowley, *Journal of Nonlinear Science* **25**, 1307 (2015).
- ¹⁸M. O. Williams, M. S. Hemati, S. T. M. Dawson, I. G. Kevrekidis, and C. W. Rowley, *IFAC-PapersOnLine* **49**, 704 (2016).
- ¹⁹S. Das and D. Giannakis, *Journal of Statistical Physics* **175**, 1107 (2019).
- ²⁰S. Pan and K. Duraisamy, *Chaos* **30**, 073135 (2020).
- ²¹S. Das and D. Giannakis, *Applied and Computational Harmonic Analysis* **49**, 573 (2020).
- ²²F. Takens, in *Dynamical Systems and Turbulence, Warwick 1980*, Lecture Notes in Mathematics, Vol. 898, edited by D. A. Rand and L.-S. Young (Springer, 1981) pp. 366–381.
- ²³J.-N. Juang and R. S. Pappa, *Journal of Guidance, Control, and Dynamics* **8**, 620 (1985).
- ²⁴Y. H. Hua and T. K. Sarkar, *IEEE Transactions on Acoustics, Speech, and Signal Processing* **38**, 814 (1990).
- ²⁵H. Arbabi and I. Mezić, *SIAM Journal on Applied Dynamical Systems* **16**, 2096 (2017).
- ²⁶S. Le Clainche and J. M. Vega, *SIAM Journal on Applied Dynamical Systems* **16**, 882 (2017).
- ²⁷S. Pan, N. Arnold-Medabalimi, and K. Duraisamy, *Journal of Fluid Mechanics* **917**, A18 (2021).
- ²⁸P. J. Schmid, *Annual Review of Fluid Mechanics* **54**, 225 (2022).
- ²⁹E. Bronstein, A. Wiegner, D. Shilo, and R. Talmon, *Chaos* **32**, 123127 (2022).
- ³⁰J. Rissanen, *Automatica* **14**, 465 (1978).
- ³¹G. Schwarz, *The Annals of Statistics* **6**, 461 (1978).
- ³²M. Wax and T. Kailath, *IEEE Transactions on Acoustics, Speech, and Signal Processing* **33**, 387 (1985).
- ³³D. Sashidhar and J. N. Kutz, *Philosophical Transactions of the Royal Society A* **380**, 20210195 (2022).
- ³⁴S. T. M. Dawson, M. S. Hemati, M. O. Williams, and C. W. Rowley, *Experiments in Fluids* **57**, 42 (2016).
- ³⁵R. Penrose, *Mathematical Proceedings of the Cambridge Philosophical Society* **52**, 17 (1956).
- ³⁶J. C. A. Barata and M. S. Hussein, *Brazilian Journal of Physics* **42**, 146 (2012).
- ³⁷P. Stoica and Y. Selén, *IEEE Signal Processing Magazine* **21**, 36 (2004).
- ³⁸M. R. Jovanović, P. J. Schmid, and J. W. Nichols, *Physics of Fluids* **26**, 024103 (2014).
- ³⁹J. L. Proctor, S. L. Brunton, and J. N. Kutz, *SIAM Journal on Applied Dynamical Systems* **15**, 142 (2016).
- ⁴⁰S. Pan and K. Duraisamy, *SIAM Journal on Applied Dynamical Systems* **19**, 480 (2020).
- ⁴¹Y.-I. Segman, A. Amar, and R. Talmon, *arXiv preprint arXiv:2502.17047* (2025).
- ⁴²Y.-I. Segman, A. Amar, and R. Talmon, in *Proceedings of EUSIPCO 2025* (2025) pp. –.
- ⁴³M. J. Colbrook and A. Townsend, *Communications on Pure and Applied Mathematics* **77**, 221 (2024).
- ⁴⁴M. J. Colbrook, L. J. Ayton, and M. Szöke, *Journal of Fluid Mechanics* **955**, A21 (2023).
- ⁴⁵D. S. Mackey, N. Mackey, C. Mehl, and V. Mehrmann, *SIAM Journal on Matrix Analysis and Applications* **28**, 971 (2006).
- ⁴⁶K. Soundararajan, *American Mathematical Monthly* **126**, 409 (2019).
- ⁴⁷Y. Harris, “Geometric-spectral framework for order detection in delay-embedded dmd,” (2026).
- ⁴⁸E. J. Candès and C. Fernandez-Granda, *Communications on Pure and Applied Mathematics* **67**, 906 (2014).
- ⁴⁹S. Kunis, D. Potts, and M. Tasche, *Linear Algebra and its Applications* **500**, 283 (2016).